Trace element characteristics of magnetite: Constraints on the genesis of the Lengshuikeng Ag–Pb–Zn deposit, China

Youqiang Qi [a,*], Ruizhong Hu [a], Jianfeng Gao [a], Wei Gao [a], Haotian Gong [a,b]

[a] State Key Laboratory of Ore Deposit Geochemistry, Institute of Geochemistry, Chinese Academy of Sciences, Guiyang 550081, China
[b] University of Chinese Academy of Sciences, Beijing 100049, China

ARTICLE INFO

ABSTRACT

Magnetite occurs as an ore mineral in many types of deposits and its trace element characteristics can be used to fingerprint various types of mineral deposits and distinguish different ore forming processes. The Lengshuikeng Ag–Pb–Zn deposit (LSKD) is one of the largest silver deposits in China, but the ore forming processes involved in its formation are still unclear. In this study, magnetites from six representative samples of different mineralization types were examined. Their trace element contents were analyzed using in situ laser ablation inductively coupled plasma mass spectrometry (LA–ICP–MS), to better understand the genesis and evolution of the ore-forming fluids responsible for Ag–Pb–Zn mineralization. The studied magnetites were divided into two types based on their spatial occurrence, associated minerals and distinctive textures. Type A magnetites are large, display subhedral to euhedral forms and appear inclusion-free. They coexist with siderites and formed early, preceding the formation of surrounding sulphides. Type B magnetites are small, exhibit irregular and anhedral forms that feature as wall-rock alterations, and were formed during the main mineralization stage. They coexist with main-stage sulphides and Fe-Mn-bearing carbonate minerals, in which Mn content increases corresponding to the evolution of the mineralization process. Generally, magnetites from the LSKD contain low amounts of Ti and V, and widely variable Al and Mn contents, which resulted from multiple influxes of low-temperature hydrothermal fluid. Type A magnetites are inferred to have formed paragenetically early at relatively high temperatures without coeval precipitation of base-metals. Conversely, Type B magnetites are interpreted to have formed during the early (B1, stage 1) and main (B2, stage 2) stages of Ag–Pb–Zn mineralization under alteration and dissolution–reprecipitation processes (DRP) from the later ore-forming hydrothermal fluids. Trace element characteristics of magnetite suggest the late hydrothermal fluid was characterized by low temperatures, and was enriched of Cl and Mn. The wide range of contents of trace elements (e.g. Ga, Mo and Sn) in magnetite that underwent DRP can be explained by different wall-rock types and water/rock ratios. Characteristics of the late hydrothermal fluids, including those from detailed microscopic observations, indicate that the ingress of Ag, Pb and Zn occurred as metal–Cl complexes, and that dissolution of early Fe, Pb, and Zn sulphides supplied the S required for the final precipitation of silver.

1. Introduction

Magnetite is a common mineral in igneous, metamorphic, and sedimentary rocks and can occur in various types of deposits (Dupuis and Beaudoin, 2011). Numerous studies have shown that certain trace element concentrations, such as Al, Ti, Mg, Mn, Zn, Cr, V, Ni, Co and Ga in magnetite are controlled by physico-chemical conditions (Carew, 2004; Singoyi et al., 2006; Beaudoin and Dupuis, 2009; Rusk et al., 2009; Chen et al., 2015a, 2015b, 2020; Dupuis and Beaudoin, 2011; Dare et al., 2012; Nadoll et al., 2012, 2014; Huang et al., 2013, 2014, 2015; Hu et al., 2014). The chemical composition of magnetite can therefore be used to fingerprint mineral deposit types, and distinguish their ore-forming processes. As a result, trace element analysis of magnetite has become an increasingly informative procedure in the study of different deposit types and their genesis.

Most studies of the chemical composition of magnetites have classified deposits according to magmatic genetic settings (e.g., Fe–Ti–P deposits, andesite, and I-type granite), high-temperature hydrothermal settings (>500 °C, e.g., iron–oxide–copper–gold (IOCG) deposits), or low-temperature hydrothermal settings (<500 °C, e.g., calcic Fe-skarn

---

* Corresponding author.
  E-mail address: qiyouqiang@mail.gyig.ac.cn (Y. Qi).

deposits, banded iron formation (BIF) and carbonate alteration in serpentinites) (Nadoll et al, 2012; Nadoll et al., 2014; Huang et al., 2013, 2014, 2015; Dare et al., 2014). Nevertheless, owing to the rarity of magnetite occurrence in Pb–Zn deposits (Nadoll et al., 2012; Leach et al., 2005), few studies of magnetite from Pb–Zn–(Ag) deposits have been performed (Nadoll et al., 2012). As a result, the genesis of such magnetites and their relationship to Ag–Pb–Zn mineralization remain unclear.

An increasing number of studies have reported that magnetite is highly susceptible to subsequent hydrothermal alteration, and then forms a secondary magnetite (Hu et al., 2014, 2015; Huang et al., 2019). For instance, the coupled dissolution–reprecipitation process (DRP) of magnetite is critical to the formation of high grade and quality iron ores in the Chengchao deposit, China (Hu et al., 2014). Hence, whether magnetite that occurs in epithermal Ag–Pb–Zn deposits was directly precipitated from hydrothermal fluids or underwent DRP resulting from multiple hydrothermal fluids, remains unclear and debated.

The Lengshuikeng deposit (LSKD), located in Jiangxi Province of South China, is an important epithermal Ag–Pb–Zn deposit, and constitutes one of the largest single sets of primary Ag orebodies in China (Mao et al., 2013, Qi et al., 2015). >40 Mt of ores with an average grade of 2.11% Pb, 2.61% Zn and 205 g/t Ag are contained in the LSKD (Wang et al., 2014). There are two types of orebody in the LSKD. One type comprises veins, veinlets and disseminated ores formed in porphyry granite intrusions that are exposed predominantly in the Yinluling, Baojia, and Yinzhushan ore fields. The other type consists mainly of massive, disseminated and vein-bound ores sandwiched within volcaniclastic rocks as evident in the Xiabao, Yinkeng, Yinglin and Xiaoyuan ore fields. Previous research has focused primarily on the geological characteristics, mineralization, wall-rock alteration, fluid inclusions, and geochemistry of the two types of Ag–Pb–Zn mineralization in the LSKD (Deng, 1991; Meng et al., 2007a; Wang et al., 2010, 2014). However, the specific mechanism of Ag–Pb–Zn mineralization and the characteristics of the ore-forming fluids remain poorly understood. Moreover, magnetite is widely developed in two types of orebody in the LSKD, and its genesis remains controversial. Some studies have suggested that the magnetite resulted from the interaction between ore-bearing granite porphyry and carbonate host rocks (Meng et al.,

2007a). However, many microscopic features exhibited by the magnetites indicate a magmatic hydrothermal origin. Furthermore, the particular metallogenic mechanisms that resulted in large-scale Ag enrichment in the LSKD are still unclear (Lu et al., 2012; Wang et al., 2014). The widely occurring magnetite and its geochemical characteristics should provide important insights into the formation mechanisms of the deposit.

For the present study, magnetites from both orebody types in the LSKD were selected. The magnetite textural and compositional data were interpreted to establish the genesis and evolution of the magnetite, leading to better understandings of the ore-forming fluids responsible for Ag mineralization. Comparisons of magnetite compositions from this study with those of magnetite-bearing mineral deposits around the world were also performed to assess similarities with magnetite from other deposits and genetic settings. This study highlights the usefulness of textural characterization conducted prior to in situ chemical analysis.

2. Regional geology

The Wuyi Cu–Pb–Zn metallogenic belt is regarded as one of the 19 key metallogenic belts in China (Chen, 2006; Yu et al., 2008a, 2008b). Its northern part is adjacent to the Gan–Hang Tectonic Belt (GHTB), and is characterized by regional E–W-trending basement uplift, and also includes a prominent NNE-trending series of Mesozoic volcanic basins, including the Dongxiang, Tianhuashan, Huangangshan, and Lizikeng (Tongboshan) basin (Fig. 1, Su et al., 2013). Several Pb–Zn deposits, such as the Lengshuikeng, Xiongjiashan, Shengmikeng, Jiaotang and Jinzhuping deposits, have developed within these volcanic basins (Luo et al., 2009; Su et al., 2013; see Fig. 1), and have attracted considerable geological research attention (Liu et al., 1994; Ding et al., 2005; Meng et al., 2007b; Wang et al., 2010).

The northern Wuyi area (NWA) is composed of Precambrian basement overlain by Phanerozoic sedimentary strata. The Precambrian units include greenschist–facies metamorphic rocks dated at 1000–800 Ma (Li et al., 1996; Shu and Charvet, 1996; Zhou et al., 2002; Shu et al., 2009). The Cambrian and Ordovician stratas comprise mainly sandstone, mudstone, and carbonaceous mudstone, but Silurian sedimentary rocks are absent in this region. The Devonian, Carboniferous, and
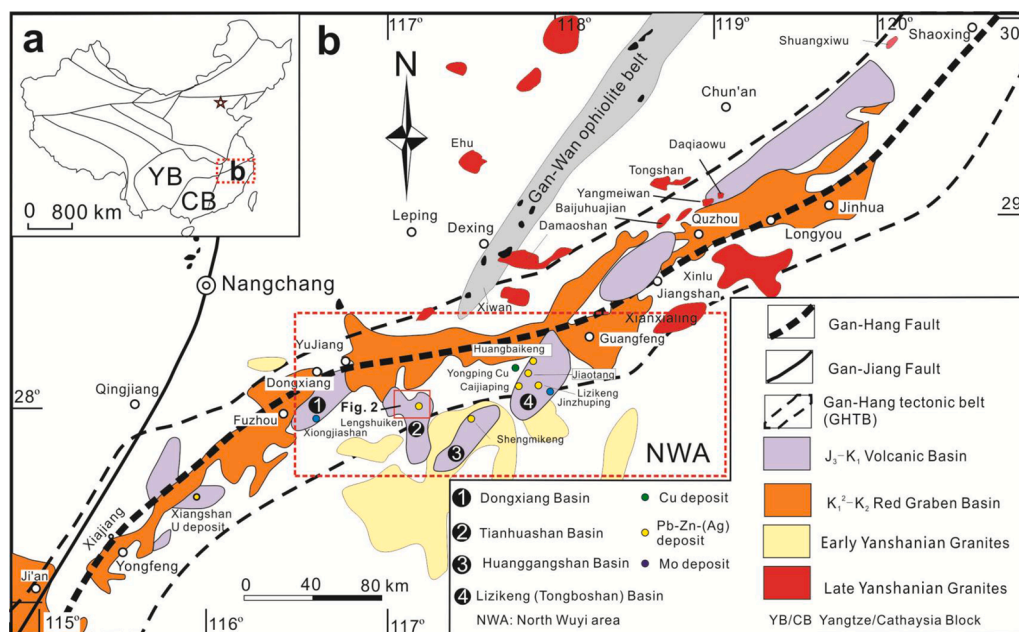

Fig. 1. (a) Simplified map of China; (b) Geological map (dashed red rectangle in Fig. 1a) of the Gan–Hang tectonic belt (GHTB) and volcanic basins in the North Wuyi Area (NWA), South China (modified from Qi et al., 2016). (For interpretation of the references to colour in this figure legend, the reader is referred to the web version of this article.)

Permian strata comprise shallow-marine- to littoral-facies clastic rocks, limestone and dolomite. The Lower Triassic series consist of muddy limestone and shale. Middle Triassic strata are absent in most areas of the NWA.

The NWA underwent a long and complex geodynamic evolution from the Proterozoic to Mesozoic, including Neoproterozoic continental amalgamation between the Yangtze and Cathaysia blocks (Li et al., 2008), an early Palaeozoic orogeny in South China (Li et al., 2010a, 2010b; Yu et al., 2012), and several Indosinian (late Permian to Triassic) and Yanshanian (Jurassic to Cretaceous) tectonothermal events (Lu et al., 2007; Mei, 1998; Wang et al., 2013; Yu et al., 2012). Among these events, the Yanshanian one was the most extensive, and created the highest stress intensity. The regional Cu–Pb–Zn–Ag–U–W polymetallic mineralizations are thought to have been closely related to the Yanshanian magmatic activity (Liu et al., 1994; Yang et al., 2004), especially the volcanic rocks that host most of the metallic ore deposits in the GHTB and NWA (see Fig. 1b; JXBGMR, 1984, 1997; Liu et al., 1994; Yang et al., 2004). Both the Yanshanian magmatism and hydrothermal mineralization were dominantly controlled by NE- to NNE-trending faults and fractures. In the Lengshuikeng region, two major NE-trending faults (F_1 and F_2) control the localization of volcanic and subvolcanic rocks, as well as that of sulphide mineralization (Fig. 2).

3. Deposit geology

The Lengshuikeng ore district is composed of stratified sedimentary and volcanic–sedimentary rocks as well as subvolcanic and other intrusive bodies of Neoproterozoic to Cretaceous age (Fig. 2). Ediacaran biotite schists and gneisses, in combination with metabasic rocks (Z_2l) crop out in the northwestern part of ore district (Fig. 2). Lower Carboniferous (C_1z) rocks crop out in the northern part, and consist of mica schists in the lower part, quartz sandstones and conglomerates in the middle part, and quartz sandstones, siltstones, and tuffaceous shales in the upper part.

The Ag–Pb–Zn mineralization is hosted in Jurassic calc-alkaline granite porphyry, as well as in volcanic-sedimentary rocks including the overlying Ehuling and underlying Daguding formations (Figs. 2 and 3). The Daguding Formation (J_{3d}) is composed of andesite, rhyolitic tuffs, and tuffaceous siltstone, whereas the Ehuling Formation (J_{3e}) is composed of tuffs, rhyolite, tuffaceous siltstone, sandstone, and Mn- and Fe-rich carbonates. Zircon U–Pb dating for the Daguding and Ehuling formations in the LSKD yielded eruption ages of 157–155 Ma (e.g., Meng et al., 2012; Sun et al., 2014). The Jurassic–Cretaceous intrusions developed in the LSKD can be divided into two main intrusion phases (Su et al., 2013). The early phase is represented by Late Jurassic granite porphyry ($\gamma\pi$) with zircon U–Pb ages of 162 to 156 Ma (Meng et al., 2007a; Zuo et al., 2010; Qi et al., 2020), which is distributed mostly in the interior of the Tianhuashan volcanic basin and associated with the Ag–Pb–Zn mineralization in the LSKD (Fig. 2). The later intrusive activity is represented by Early Cretaceous intrusions, including a quartz syenite porphyry ($\theta\xi\pi$), rhyolite porphyry ($\lambda\pi$), and feldspar granite porphyry ($K\gamma\pi$), with zircon U–Pb ages ranging from 142 to 140 Ma (Fig. 2; Su et al., 2014), and which are distributed chiefly in the deposit district and its periphery.
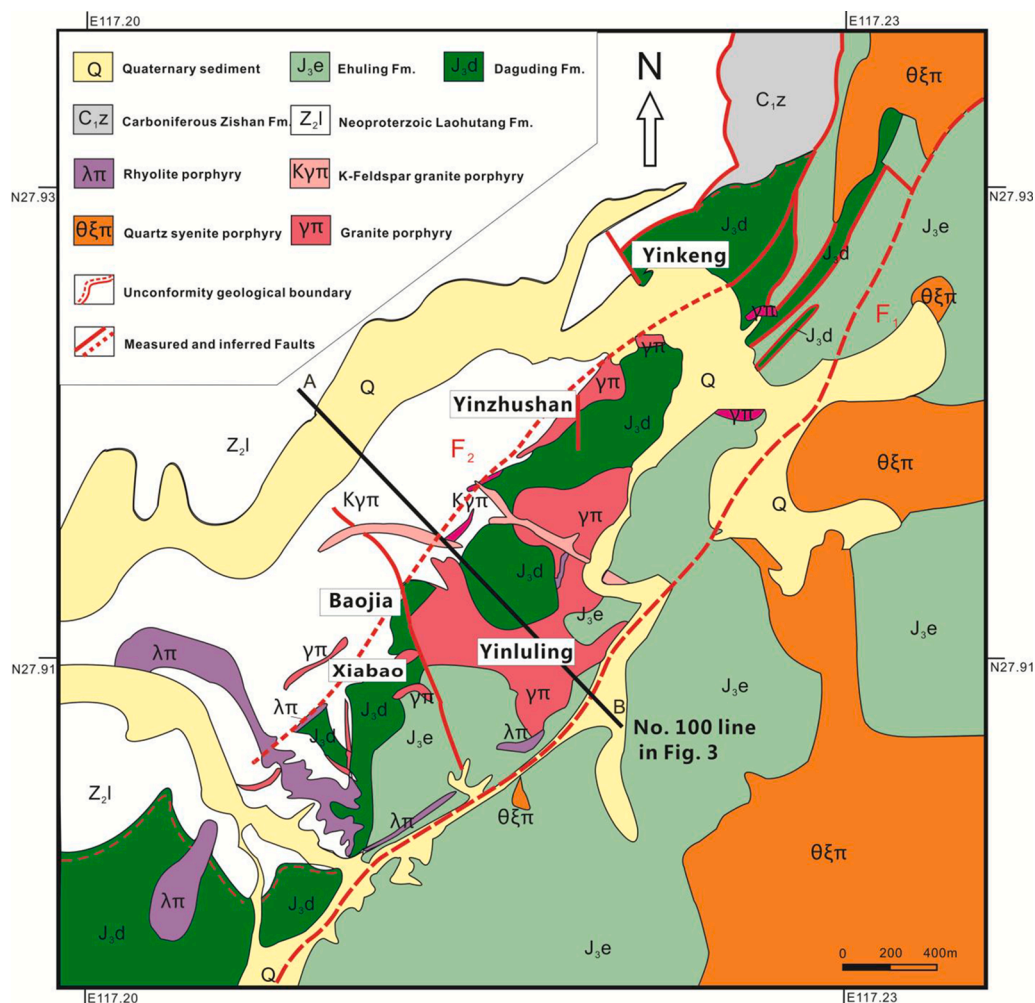

Fig. 2. Geological map of the Lengshuikeng Ag–Pb–Zn deposit area (modified after Meng et al., 2007a, 2007b).
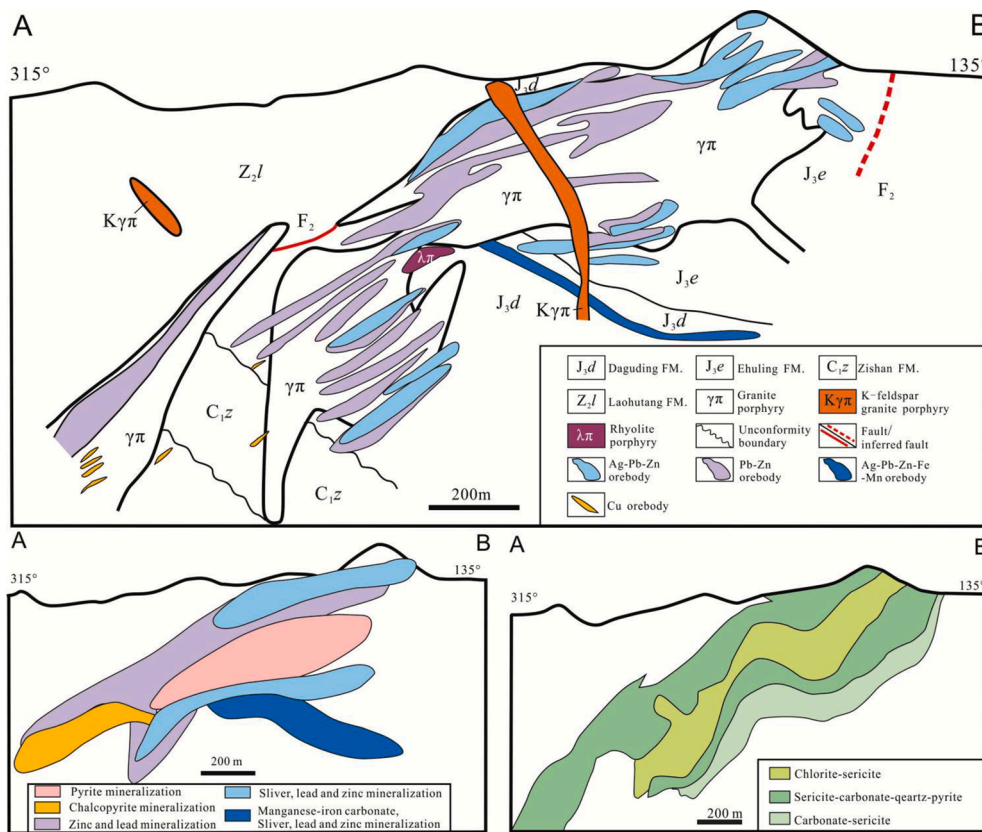
Fig. 3. Cross-section showing (a) geological features, (b) mineralization zonation, and (c) alteration zonation along No. 100 line section in the LSKD (adapted from figures produced by the No. 912, 1997.

Two types of mineralization, including porphyry- and stratabound-type, occur in the LSKD (Fig. 3a). The porphyry-type mineralization is hosted mainly in granite porphyry, showing zonation of metallic elements from Cu at depth, through Pb–Zn–Ag, to Ag–Pb–Zn in the shallow contact zone with volcaniclastics (Fig. 3b). The Yinluling and Baojia orebodies contain the largest ore reserves, and were therefore the initial focus of mineralization research in the LSKD (Lei et al., 2012; Meng et al., 2009; Wang et al., 2011; Zuo et al., 2009). The stratabound-type mineralization is sandwiched within the Daguding sequence of volcaniclastic rocks, and displays a close association with Fe–Mn carbonate layers as well as a conformable contact with the host volcanic-sedimentary rocks (Fig. 3a). The Xiabao ore field in the southwestern part of the LSKD contains the largest metal reserves of stratabound mineralization in this region (Li and Jiang, 2016). The disseminated- and vein-type textures are developed mainly in porphyry-type mineralization, whereas the massive and veinlet-type textures occur predominantly in stratabound-type mineralization. Details of characteristics of the two mineralization types are listed in Table 1. The major types of alterations are chloritization, sericitization, and carbonatization, which are developed chiefly in the porphyry-type mineralization. In general, the spatial distribution of orebodies in the porphyry is in accordance with the occurrence of alteration and superposition. The Cu-rich orebodies are closely associated with chlorite and sericite alteration in the inner zone of the porphyry granite, whereas the Pb–Zn–Ag orebodies are hosted mainly in the sericitization, carbonatization, and silicification zones. The Ag–Pb–Zn orebodies that occur alongside carbonatization and sericitization are located in the peripheral (or distal) zone (Fig. 3b, c). The major ore minerals in all types of mineralization are typically identical, and contain mainly sphalerite, galena, pyrite and silver minerals (acanthite and native silver). The main sulphide mineralization in the stratabound and porphyry ores has been divided into three stages: stage 1, pyrite–chalcopyrite–sphalerite; stage

Table 1
Ore body characteristics in Lengshuikeng Ag-Pb-Zn ore field.

Items	Ore body hosted in porphyry granite	Ore body hosted in volcaniclastic rocks
Location	Yinluling, Baojia, Yinzhushan	Xiabao, Yinkeng, Yinglin, Xiaoyuan
Wall rocks	porphyry granite and contact zone	volcanic clastic, carbonate and siliceous rocks
Ore body morphology	lentoid	stratiform-like, regular lentoid
Ore minerals	Py, Sph, Gn, Mt, Aca, Slv	Fe-Mn Carb., Mt, Py, Sph, Gn, Aca, Slv, Hem
Gangue mineral	Qtz, Or, Fl, Chl, Ser	Dol, Qtz, Jd
Ore texture	disseminated, vein	massive, veinlet
Wallrock alteration	chloritization, sericitization, carbonatization, pyritization and silication	carbonatization, weak sericitization and linear chloritization
Ore-forming elements	Ag-Pb-Zn-Cd-Cu-Au	Ag-Pb-Zn-Cd-Au

Mineral abbreviations: Py = pyrite, Sp = sphalerite, Gn = galena, Aca = acanthite, Slv = native silver, Fe-Mn Carb. = Fe-, Mn-rich carbonate minerals (siderite and rhodochrosite), Mt = magnetite, Hem = hematite, Qtz = quartz, Or = orthoclase, Fl = plagioclase, Chl = chlorite, Ser = sericite, Dol = dolomite, Jd = jadeite.

2, silver minerals–galena–sphalerite; and stage 3, pyrite–quartz–calcite (Wang et al., 2014). Mineral paragenesis of the two mineralization types is shown in Fig. 4.

The magnetite is typically dispersed in both types of mineralization. The magnetite has been identified as being distributed generally in Fe- and Mn- rich carbonate ores near the porphyry (Meng et al., 2007a, 2007b). However, our field investigation shows that the distribution of magnetite is not only limited to the porphyry contact zone, but is also

Minerals	Early stage	Main sulphide period		
		Stage 1	Stage 2	Stage 3
Siderite	▬▬▬	▬▬▬▬▬▬▬▬▬▬		
Manganosiderite	▬▬▬▬▬▬▬▬▬			▬▬
Pyrite	▬▬▬	▬▬▬	▬▬	▬▬
Arsenopyrite	▬▬▬			
Quartz	▬▬▬	▬▬	▬▬	
Magnetite	▬▬▬	▬▬	▬▬	
Chlorite		▬▬	▬▬	
Chalcopyrite		▬▬	▬▬	
Pyrrhotite		▬▬		
Sphalerite		▬▬	▬▬	▬▬
Galena		▬▬	▬▬	▬▬
Acanthite			▬▬	
Native silver			▬▬	
Calcite				▬▬

Fig. 4. Mineral paragenesis of the Lengshuikeng Ag–Pb–Zn deposit.

developed in veins/veinlets in the granite porphyry, and veins/veinlets and massive ores in the stratabound orebody. On the whole, the occurrence of the magnetite is closely related to the presence of Fe- and Mn-rich carbonate minerals. Further details are presented in the Section 5.

4. Analytical methods

4.1. SEM–BSE–EDS

Scanning electron microscopy–backscattered electron (SEM–BSE) images and energy dispersive spectrometer (EDS) mapping were performed using field emission–SEM (FE–SEM, JEOL JSM-7800F) at the State Key Laboratory of Ore Deposit Geochemistry, Institute of Geochemistry Chinese Academy of Sciences (SKLODG IGCAS), Guiyang, China. These analyses were conducted using an accelerating voltage of 25 kV and a beam current of 10nA.

4.2. LA–ICP–MS

Magnetite laser ablation-inductively coupled plasma–mass spectrometry (LA–ICP–MS) analyses were conducted using a 193 nm Geolas laser coupled to a Varian 820-MS ICP–MS instrument at the Advanced Analytical Centre, James Cook University (AAC JCU), Townsville, Australia. The quantitative analyses were performed by ablating spots of ~44 μm in size on both magnetites and standards. The laser repetition rate was typically 10 Hz and the laser beam energy directed at samples was maintained between 5 and 6 J/cm². The analysis time for each sample was 70 s, comprising a 30 s measurement of background (laser off) and a 40 s analysis (laser on). Ablation occurred in an atmosphere of pure He flowing at a rate of 0.8 l/min. Immediately pasting the ablation point within the cell, He carrier gas was mixed with Ar (0.95 l/min) for improved efficiency of aerosol transport. Production of molecular oxide species ($^{232}Th^{16}O^+/^{232}Th^+$) was maintained at levels below 0.5%, and the U/Th ratio was nearly equal to 1 for standard reference material NIST610.

For magnetite, a total of 32 isotopes were measured. Each analysis was performed in time-resolved mode which involves sequential peak hopping through the mass spectrum. Analyses were calibrated against GSE-1G glass for all elements except P, which was calibrated against GSD-1G glass (GeoReM preferred values: http://georem.mpch-mainz.gwdg.de/). MPI-DING GOR-128 g (natural komatiitic glass) and in-house standard BC28 (natural massive magnetite, Barnes et al., 2004; Dare et al., 2014) were used as secondary standards to check the accuracy of this method. The theoretical mole ratio of Fe in magnetite was used as an internal calculated standard. Glitter software v4.4 (http://www.glitter-gemoc.com/) was used for data reduction. Accuracy was better than 20% for most elements (Dare et al., 2014).

5. Samples and ore petrography

During this study, six representative samples of disseminated, vein, and massive ores were selected from the Yinluling and Xiabao orebodies. Details of sample locations and description are shown in Table 2. Photographic depictions of sample-specific petrographic features were obtained prior to LA–ICP–MS analyses (see Fig. 5). Samples XBYH14-08, XBYH14-21, and XBYH14-18a were collected from a stratabound-type

Table 2

Ore samples, location and description in Lengshuikeng Ag-Pb-Zn ore field.

Sample No.	Location	Description
KD14-17	Xiabao	Massive texture ore with Py + Sp + Gn + Po + Mt cut by late Qtz veinlet
XBYH14-08	Xiabao	Massive ore with Qtz + sulphides (Py+Sp+Gn) + Carbonate minerals
XBYH14-18a	Xiabao	Veinlet texture ore with Fe-Mn carbonate minerals + Py + Mt
XBYH14-21	Xiabao	Disseminated texture ore with Mt + Py + Gn + Sp
YLL14-37-1	Yinluling	Stockwork texture ore with Py + Mt + Fe-Mn carbonate minerals
YLL14-37-2	Yinluling	Stockwork texture ore with Py + Mt + Fe-Mn carbonate minerals

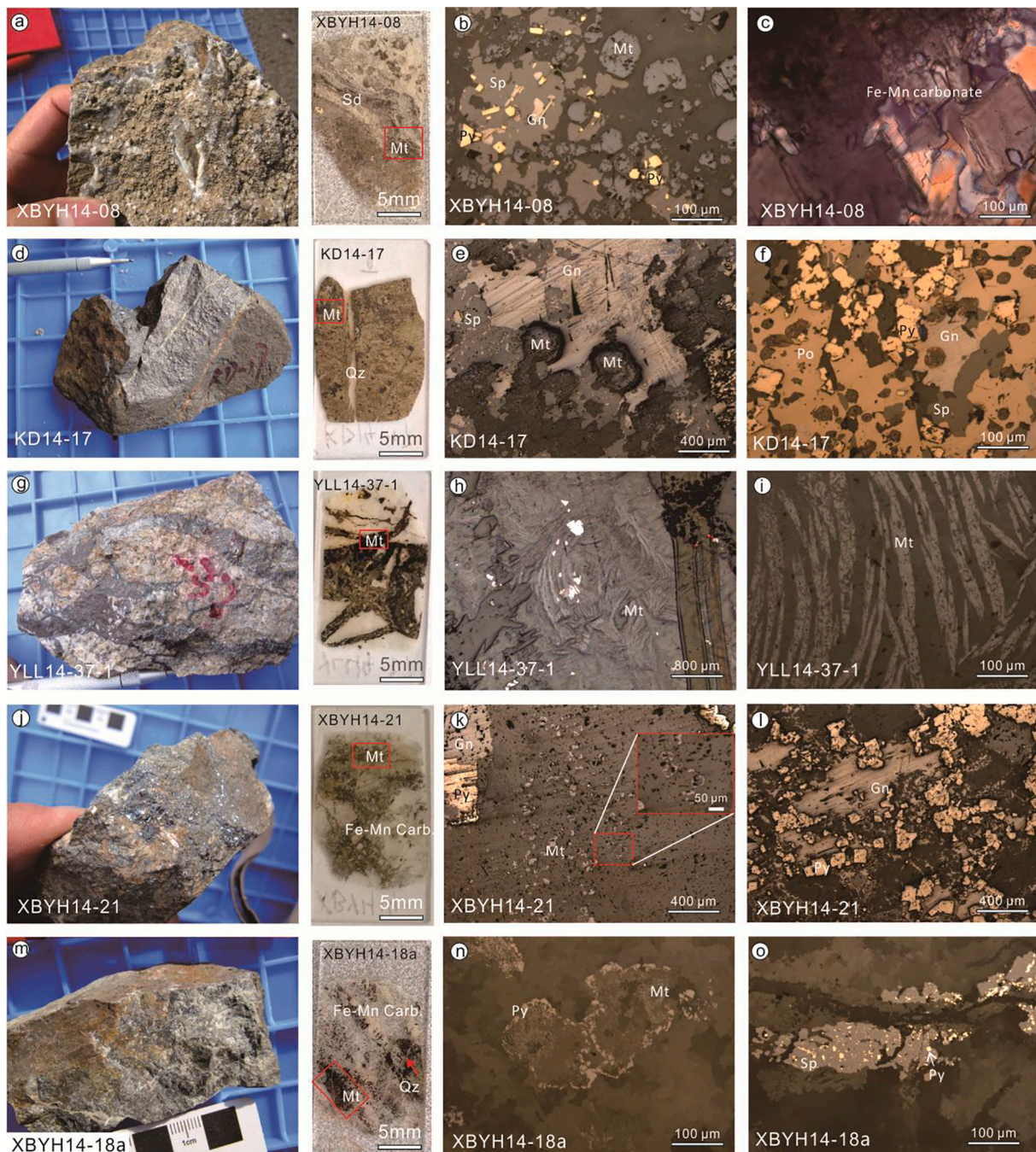Mineral abbreviations are same as in Table 1.

Fig. 5. Photographs (a, d, g, j, and m) and reflected-light photomicrographs (the remaining panels) showing structures, textures, and mineralogies of representative samples selected from the Lengshuikeng Ag–Pb–Zn deposit. Massive texture sample XBYH14-08 (a), with grains of subhedral magnetite surrounded by subhedral galena and sphalerite, and euhedral pyrite, all suspended in Fe–Mn carbonate minerals (siderite and rhodochrosite) (b), and carbonate minerals with euhedral rhombus indicating its late stage of formation (c). Massive-texture sample KD14-17 with sulphides-cross cut by late quartz veins (d), including subhedral magnetite surrounded by subhedral galena and sphalerite that exhibits 'chalcopyrite disease' texture (e), and containing pyrrhotite, sphalerite, pyrite, and galena (f). Vein-texture sample YLL14-37-1 (g), with plumose laths of magnetite and anhedral pyrite (h), and regularly arranged magnetite with lathy shapes enclosed by carbonate minerals (i). Disseminated-texture sample XBYH14-21 with Fe–Mn carbonate minerals (siderite and rhodochrosite) (j), magnetite exhibiting a scattered and disseminated texture unattached to specific sulphides (k), and main sulphides, including pyrite, galena and sphalerite, all suspended in carbonate minerals (l). Veinlet texture sample XBYH14-18, containing abundant Fe–Mn carbonate minerals (m), anhedral magnetite encased in rims of pyrite (n), and sphalerite and pyrite cross-cut by a late quartz vein (o). Mineral abbreviations: Mt = magnetite, Py = pyrite, Sp = sphalerite, Gn = galena, Clp = chalcopyrite, Po = pyrrhotite, Qtz = quartz, and Fe-Mn Carb. = Fe–Mn-rich carbonate minerals (siderite and rhodochrosite).

orebody in the Xiabao ore field and, and exhibit veinlet and disseminated textures (Fig. 5a, j and m). Sample KD14-17 was also collected from the Xiabao ore field, and shows a massive texture (Fig. 5d). Samples YLL14-37-1 and YLL14-37-2 exhibiting vein and stockwork textures, were collected from porphyry-type orebody in the Yinluling ore

field (Fig. 5g).

Sample XBYH14-08 is composed of sphalerite, pyrite, galena, magnetite, arsenopyrite, and Fe–Mn-rich carbonate minerals (a continuous solid solution of siderite and rhodochrosite) (Figs. 5c and 6b, c). The magnetite is developed in an area of the sample shown with a red

square in Fig. 5a. Magnetite grains exhibit euhedral shapes with sizes of up to 100 μm, and are commonly surrounded by subhedral galena and sphalerite, and by euhedral pyrite (Figs. 5b, and 6b), indicating that they were formed paragenetically early. Some magnetite grains display triple-junction textures (120°) which is indicative of textural equilibration (Hu et al., 2015), as well as curved margins (Fig. 6c). Mn-rich carbonate grains appear in micro-fractures and at the margin of the magnetite grains, whereas siderite grains occur well away from magnetites (Fig. 6c). Those features indicate that the magnetites were altered by late Mn-rich hydrothermal fluids, although this process was limited, and did not alter the core of the magnetite grains.

Sample KD14-17 consists predominantly of sphalerite, pyrite, galena, pyrrhotite, arsenopyrite and magnetite (Figs. 5d, e, f, and 6a). The ores containing these minerals have been cross-cut by late quartz veins. The magnetite is developed in an area shown by a red square in Fig. 5d. Microscopic observations show that euhedral magnetites (up to 300 μm) are enclosed by subhedral galena and sphalerite (Fig. 5e). These features indicate that the magnetites were formed earlier than sulphides during the main stages of mineralization (stages 1 and 2). Given the lack of co-mineralized silicate minerals, these magnetites are inferred to have formed through hydrothermal precipitation of minerals in open spaces. In combination with the characteristics of trace elements, the origin of the magnetites is discussed in detail in Section 7.1 below.

Sample XBYH14-18a comprises minerals similar to those in XBYH14-08. However, in XBYH14-18a, pyrites rim with anhedral magnetite grains, and irregular-shaped sphalerites contain disseminated pyrites (stage 1), and all of the sulphides are in direct contact with Fe- and Mn-rich carbonate minerals (Fig. 5n, o). These features indicate that the magnetite was strongly influenced by the deposition of later-formed sulphides during the main stages of mineralization and by extensive carbonate formation.

Magnetite grains from sample XBYH14-21 occur in Mn-rich carbonate minerals, exhibit scattered, disseminated distributions, and are not in contact with surrounding sulphides (Fig. 5j, k). These magnetites exhibit anhedral shapes with relatively small sizes (mostly < 60 μm), and some grains reveal skeleton-type textures (magnified area in the red square in Fig. 5k). This indicates the intensive influence from late Mn-rich hydrothermal fluids. Microscopic observations show that Fe- and Mn-rich carbonate minerals containing sulphide minerals (early pyrite) occur within Mn-rich carbonate minerals that are in contact with galena and feldspar (Fig. 6d). These relationships indicate that Fe- and Mn-rich carbonate minerals were formed during the early stage of mineralization (stage 1), prior to the formation of Mn-rich carbonate minerals during the main sulphide stage (stage 2). In XBYH14-21, acanthites occur at the margins of and in fractures through pyrite and galena (Fig. 7a). Elemental mapping using EDS indicates a close association between Ag, Au, As, and Sn components (Fig. 7).

Samples YLL14-37-1 and YLL14-37-2 are developed in veinlets of millimetres to centimetres width, which are infilled mainly by Fe- and Mn-rich carbonate minerals, pyrites, arsenopyrites, and plumose laths of magnetite (Figs. 5g, h, i, and 6e, f). These magnetites coexist with anhedral pyrites, and both are suspended in the Fe- and Mn-rich carbonate minerals (Fig. 5h). Euhedral arsenopyrites are developed along contact zones between veinlets and wall rock (mainly feldspar), and Fe- and Mn-rich carbonate minerals occur in the margins of arsenopyrite grains and the clearance of feldspar grains (Fig. 6f). Very tiny mineral grains (possibly acanthite) with high Ag content are distributed near Fe–Mn carbonate minerals (indicated by red arrows in Fig. 6f). In YLL14-37-1, some Fe- and Mn-rich carbonate minerals contain minor arsenopyrites, in contrast to the inclusion-free siderites (Fig. 6e). It is inferred
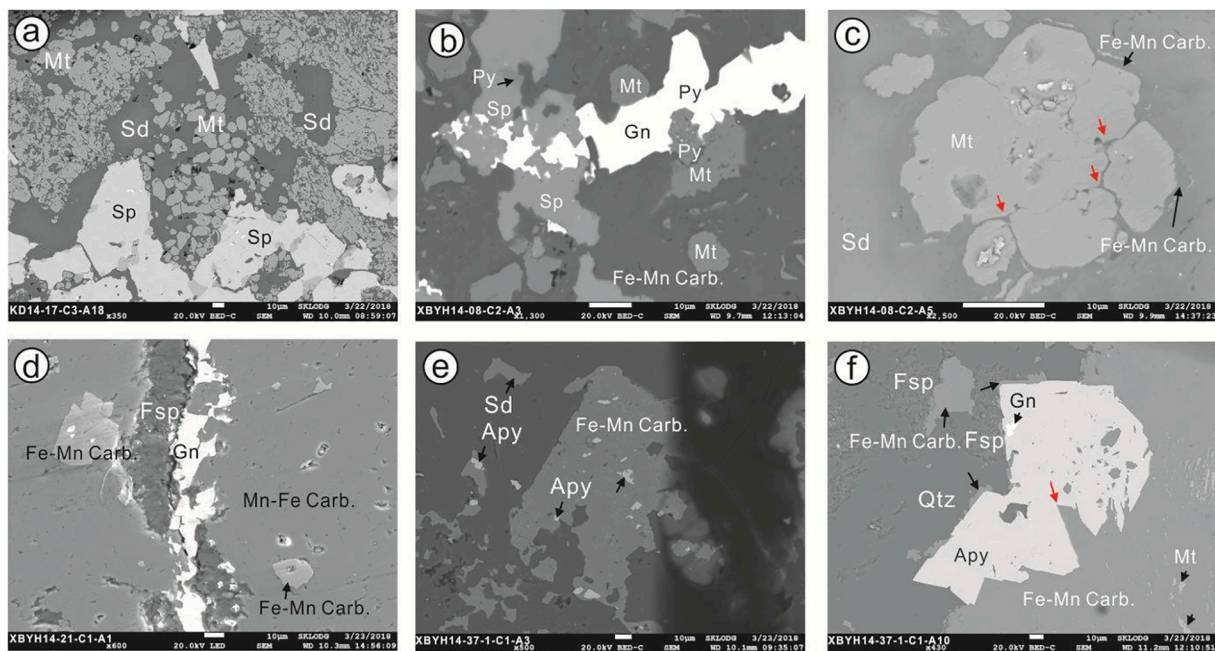

Fig. 6. SEM-BSE images (a–c, e–f) and a reflected-light photomicrograph (d) of typical mineral grains from the Lengshuikeng Ag–Pb–Zn deposit showing occurrences and textural features of magnetite, sulphides, and carbonate minerals. (a) Subhedral and euhedral magnetite and sphalerite enclosing magnetite, all suspended in siderite; (b) major sulphides (galena, pyrrhotite, and euhedral pyrite) partially enclosing early subhedral magnetite, all suspended in carbonate minerals with higher Mn content, referred to as Fe–Mn carbonate minerals to distinguish them from earlier siderite; (c) magnetite grains with triple-junction textures (120°) indicated by red arrows, and marginal curved shapes indicated by black arrows, enclosed in Mn-bearing carbonate minerals close to magnetite and Fe-rich carbonate minerals (siderite) distant from magnetite; (d) Fe–Mn carbonate grains suspended in Mn–Fe carbonate minerals, the latter close to galena and feldspar, indicating that Fe–Mn carbonate minerals formed prior to Mn–Fe carbonate minerals; (e) siderite and inclusion-rich Fe–Mn carbonate minerals that contain arsenopyrite, indicating their paragenetic sequence; (f) Fe–Mn carbonate minerals present in the margins of arsenopyrite and galena, and abundant silver distributed in a sharply defined embayment (indicated by the red arrow). Mineral abbreviations: Mt = magnetite, Py = pyrite, Sp = sphalerite, Gn = galena, Clp = chalcopyrite, Po = pyrrhotite, Apy = arsenopyrite, Acan = acanthite, Qtz = quartz, Fsp = feldspar, Sd = siderite and Fe–Mn/Mn–Fe Carb. = Fe–Mn and Mn-Fe-rich carbonate minerals (siderite and rhodochrosite). (For interpretation of the references to colour in this figure legend, the reader is referred to the web version of this article.)
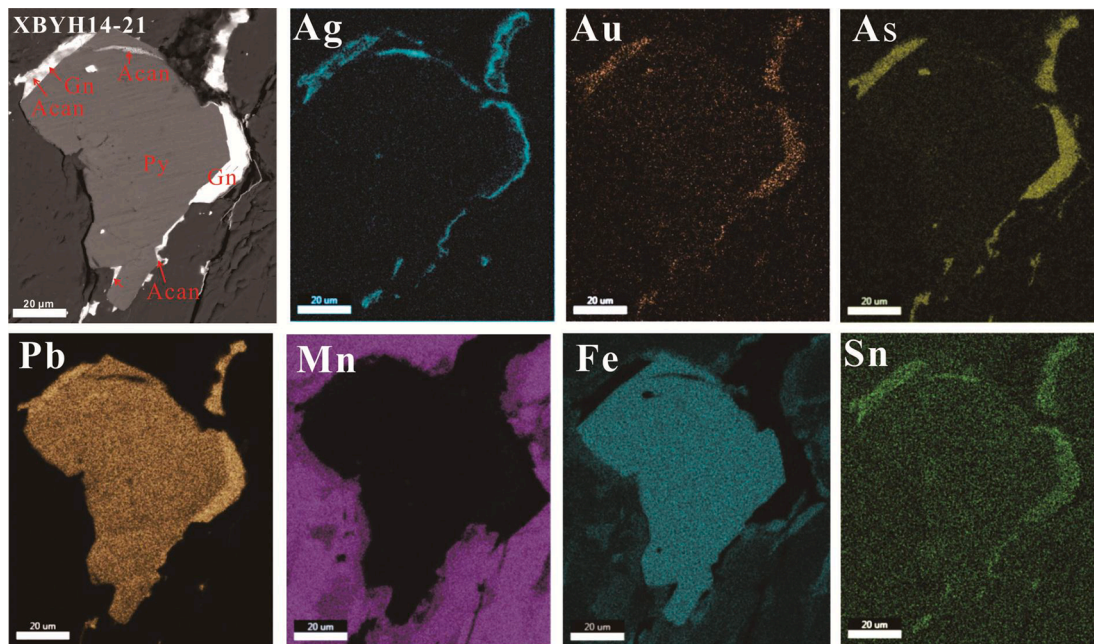
Fig. 7. SEM–BSE images displaying EDS element mapping for sample XBYH14-21. Acanthite is distributed along the rim and in fractures within early-formed pyrite and galena. Elemental mapping demonstrates close relationships between Ag and Au, As, and Sn. Mineral abbreviations as for Fig. 5.

that the magnetites were formed during the early stage of sulphide formation (stage 1, pyrite and arsenopyrite), and that they were strongly influenced by later fluids that formed sulphides and carbonates during stage 2 of mineralization.

On the basis of their spatial occurrence, associated minerals, and distinctive ore textures, the magnetites can be divided into two types irrespective of orebody types. Magnetites from samples XBYH14-08 and KD14-17 are classified as early Type A magnetites, which are large with clean subhedral to euhedral shapes, and coexist mainly with Fe-rich carbonate minerals (siderite), formed prior to the surrounding sulphides, and underwent only limited influence by late hydrothermal fluids. In contrast, magnetites from samples XBYH14-18a, XBYH14-21, YLL14-37-1 and YLL14-37-2 are classified as Type B magnetites that have irregular to anhedral shapes and altered characteristics from late fluids. These Type B magnetites appear to coexist with main-stage sulphides and Fe–Mn-bearing carbonate minerals. Furthermore, the magnetites in samples YLL14-37-1 and YLL14-37-2 affected by hydrothermal fluids mainly during early mineralization (stage 1), can be classified as Type B1, whereas those in samples XBYH14-18a and XBYH14-215 affected by hydrothermal fluids chiefly during the main mineralization (stage 2), can be classified as Type B2. Nevertheless, both types of magnetite were formed in the same ore-forming hydrothermal fluid system, as inferred from a previous investigation of sulphides from both types of orebody in the LSKD (e.g., Leng and Qi, 2018). The sequence of carbonate mineral formation is from siderite, through Fe- and Mn-rich carbonate, to Mn-rich carbonate minerals, associated with main metal mineralization. The Mn content in carbonate minerals appears to have increased over time during the mineralization process.

6. Results

A total of 32 elements were analyzed during the assessment of each magnetite sample. Contents of S, Ta, and Au were either close to or below the detection limit, or showed considerable variation in ranges, therefore, these elements are not considered further here. The mean contents of the selected major and trace elements of magnetite from different types of ores are listed in Table 3.

Smooth curves for selected elements from signal intensity versus time plots indicate the absence of other mineral inclusions in our analyzed magnetites (Fig. 8). In addition, the selection of smooth transitions was preferred when abnormal peaks occurred in the time profile in the process of raw data reduction. Hence, the magnetite elemental compositions reported in this study can be used to represent the composition of magnetites, and to trace their source and formation process.

Magnetite grains from the LSKD contain highly variable trace element contents. Type A magnetites contain 256–5709 ppm Mn, 446–5615 ppm Mg, 45–694 ppm Al, 11.7–47.2 ppm V, 17.7–85.7 ppm Ti, 0.7–12.5 ppm Ni, 11.0–8123 ppm Zn, 1.4–232 ppm Pb, 23.9–422 ppm Sn and 0.12–3.29 ppm Co. In contrast, Type B magnetites contain 111–94330 ppm Mn, 65–6837 ppm Mg, 148–8053 ppm Al, 0.2–7.7 ppm V, 0.4–11.2 ppm Ti, 0.6–5.9 ppm Ni, 19.3–1027 ppm Zn, 1.3–108 ppm Pb, 0.9–515 ppm Sn, and 0.15–0.78 ppm Co (see Table 3). In binary plots of elements and/or their ratios (Figs. 9 and 10), Type A magnetites display as distinct clusters from Type B magnetites. Generally, Type A magnetites contain higher contents of Ti and V but lower Mn. There are positive relationships between Ti and V contents in Type A magnetites (Fig. 9a), and are weak positive relationships between Mg and Mn in both types of magnetite (Fig. 9b).

Disseminated Type B magnetites from XBYH14-21 contain the highest Mn and Mo contents (Fig. 9b, c). Type A magnetites contain relatively high Sn and low Mo contents, whereas Type B magnetites from samples XBYH14-37-1 and -2 from ores with stockwork structures, contain low Sn and moderate Mo contents (Fig. 9c). Magnetites from sample XBTH14-18a contain the highest Ga contents (Fig. 9d). Contents of Al in both types of magnetite plot in similar ranges of values (Fig. 9e, f).

7. Discussion

7.1. Origin of the two types of magnetite

According to petrographic evidence (Section 5), Type A magnetites formed prior to the surrounding sulphides, are large, have subhedral–euhedral shapes, have an inclusion-free appearance, and coexist with siderite. Type B magnetites are smaller than those of Type A, coexist with sulphides and Fe- and Mn-bearing carbonate minerals, exhibit irregular and anhedral shapes, and appear to have been altered

Table 3
Trace element concentrations of magnetite analyzed by LA-ICP-MS in Lengshuikeng Ag-Pb-Zn ore field.

Sample	Spot	Si ppm	Ca ppm	Y ppm	P ppm	Pb ppm	Zr ppm	Hf ppm	Al ppm	Ge ppm	W ppm	Sc ppm	Ta ppm	Nb ppm	Cu ppm	Mo ppm	Sn ppm	Ga ppm	Mn ppm	Mg ppm	Ti ppm	Zn ppm	Co ppm	V ppm	Ni ppm	Cr ppm
XBYH14-08	C2-01	2022	3179	2.31	58.1	59.0	2.14	0.05	48.9	9.31	5.78	0.46	0.01	0.40	1.73	0.67	265	2.90	5709	4643	85.7	759	3.29	36.3	11.6	103
	C2-02	4024	368	3.48	64.6	67.3	12.8	0.16	286	3.68	1.46	0.44	0.00	0.24	6.42	0.14	23.9	16.9	791	446	70.1	367	2.23	39.0	12.5	125
	C2-03	1350	258	1.21	46.7	5.51	0.82	0.04	45.4	3.73	0.67	0.32	0.00	0.12	b.d.l.	0.22	59.8	9.6	718	699	27.1	31.6	0.12	19.9	3.43	32.9
	C2-04	3187	2680	1.82	80.2	15.6	2.13	0.03	285	14.5	4.47	0.23	0.01	0.18	0.65	0.53	305	14.0	4278	2525	26.0	452	b.d.l.	15.7	4.82	26.9
	C2-05	1554	3890	1.74	45.7	11.9	1.04	0.03	114	14.2	9.78	0.22	0.01	0.26	b.d.l.	0.41	327	10.0	3544	2164	38.7	315	0.12	20.3	4.11	54.9
	C2-06	3232	2168	1.86	40.8	57.4	2.24	0.04	344	16.3	5.33	0.23	0.01	0.17	1.18	0.58	199	14.8	4562	2018	61.9	196	0.16	28.9	3.09	49.3
	C2-07	2997	2248	4.53	38.8	174	14.9	0.25	411	16.0	6.84	0.30	0.01	0.24	87.3	0.40	149	13.7	5135	2861	49.1	316	2.09	32.9	11.3	54.2
	C2-08	1866	2270	1.54	29.2	232	3.75	0.05	91.4	9.1	3.20	0.15	0.00	0.13	8.40	0.24	164	11.8	1661	1355	38.4	150	b.d.l.	14.2	3.77	57.4
KD14-17	C3-01	3216	2507	1.44	56.4	3.64	0.44	b.d.l.	335	13.3	33.7	3.10	0.01	0.12	2.54	0.36	422	22.9	643	1077	47.7	11.9	0.24	47.2	1.28	7.04
	C3-02	3186	2461	1.49	52.6	6.18	0.85	0.02	156	13.1	20.4	1.97	0.00	0.12	573	0.17	92.1	22.4	256	1009	47.1	11.0	0.23	27.2	b.d.l.	12.2
	C3-03	3025	4184	1.38	78.0	2.88	0.32	0.01	370	12.1	19.0	1.83	0.00	0.07	b.d.l.	0.13	81.3	18.8	329	2225	36.6	11.8	0.30	17.3	b.d.l.	8.15
	C3-04	1915	16756	15.4	7239	1.45	1.62	0.07	170	4.8	21.3	2.52	b.d.l.	0.05	b.d.l.	0.15	136	12.2	448	5615	17.7	21.6	b.d.l.	11.7	0.69	10.6
	C3-05	4108	2545	2.17	64.8	20.1	3.25	0.06	556	14.2	18.3	2.91	0.00	0.05	3.69	0.63	109	22.4	293	1599	32.4	8123	b.d.l.	15.7	b.d.l.	35.9
	C3-06	2931	3245	1.59	137	4.71	0.49	0.01	179	14.5	37.7	2.65	0.00	0.09	0.99	0.10	172	19.9	345	1140	35.9	18.4	b.d.l.	17.7	b.d.l.	5.09
	C3-07	3516	6241	2.21	63.3	3.43	3.59	0.02	694	10.3	18.1	2.86	0.00	0.09	4.71	0.06	108	18.8	464	3880	33.8	11.9	b.d.l.	18.1	b.d.l.	19.2
XBYH14-18a	C1-01	6678	651	0.33	80.5	61.2	0.11	0.05	287	84.7	13.0	0.12	0.01	0.01	b.d.l.	b.d.l.	118	163	196	127	1.43	1027	0.54	5.39	1.51	9.19
	C1-02	6035	1086	0.09	24.2	29.8	0.27	b.d.l.	204	56.7	8.27	0.12	0.00	b.d.l.	b.d.l.	0.17	356	167	807	231	1.96	84.9	0.16	7.72	1.20	24.0
	C1-03	11918	142	0.09	59.7	108	0.34	0.01	1106	91.6	11.6	0.09	0.00	0.01	4.16	0.10	221	248	111	65.0	1.50	168	0.56	7.70	0.99	5.83
	C1-04	7361	1322	0.44	55.3	80.0	0.26	0.03	266	95.9	16.2	b.d.l.	0.06	0.03	b.d.l.	0.29	171	154	2876	1005	1.37	320	0.41	6.43	2.04	6.07
	C1-05	9473	3122	0.84	271	39.3	0.26	b.d.l.	488	127	17.9	b.d.l.	0.04	0.02	0.60	0.69	253	148	7448	2326	2.14	770	0.75	5.09	1.12	8.19
	C1-06	10451	2917	0.77	143	51.6	0.33	0.00	359	43.6	12.6	b.d.l.	0.02	0.05	b.d.l.	0.39	515	210	5327	2413	3.06	869	0.53	4.50	0.74	5.44
XBYH14-21	C1-01	12615	3215	1.31	22.1	18.7	0.59	0.02	8053	0.96	5.33	0.45	b.d.l.	0.05	4.59	5.67	190	10.3	70588	3839	5.41	61.8	0.71	5.51	4.91	137
	C1-02	1384	2059	0.56	31.0	2.09	0.08	0.00	177	3.74	15.2	b.d.l.	b.d.l.	0.02	1.55	3.43	78.5	3.39	43175	1418	0.39	23.9	0.47	3.71	1.70	337
	C1-03	970	358	0.22	37.3	3.11	0.07	0.00	148	4.54	16.7	0.14	0.01	b.d.l.	0.73	0.72	78.2	1.81	7294	351	1.46	57.6	b.d.l.	0.60	2.35	11.8
	C1-04	611	2284	1.71	37.9	4.61	b.d.l.	b.d.l.	163	0.66	10.2	b.d.l.	b.d.l.	0.09	b.d.l.	4.29	92.8	1.50	49930	1986	2.32	52.5	0.69	1.07	0.80	13.8
		15263	2647	0.67	53.9	1.27	0.63	0.02	3356	1.19	26.9	0.35		0.20		2.54	324	5.01	34221	3116	10.0	19.8	0.23	3.72	1.73	10.3

Table 3 (*continued*)

| Sample	Spot	Si ppm	Ca ppm	Y ppm	P ppm	Pb ppm	Zr ppm	Hf ppm	Al ppm	Ge ppm	W ppm	Sc ppm	Ta ppm	Nb ppm	Cu ppm	Mo ppm	Sn ppm	Ga ppm	Mn ppm	Mg ppm	Ti ppm	Zn ppm	Co ppm	V ppm	Ni ppm	Cr ppm
	C1-05												b.d.l.		b.d.l.											
	C1-06	1035	3137	1.01	44.2	2.58	0.13	0.00	261	1.20	14.7	0.22	b.d.l.	0.01	b.d.l.	7.97	21.3	1.95	94330	3091	2.41	24.6	0.31	3.56	b.d.l.	29.0
YLL14-37-1	C1-01	1855	11300	5.93	135	17.2	0.18	0.02	920	1.89	12.4	0.69	0.00	0.64	9.68	0.35	1.70	1.23	3958	5343	11.0	41.5	0.15	0.40	b.d.l.	11.0
	C1-02	1828	10157	6.03	178	7.83	0.16	0.02	720	1.83	11.2	0.54	0.00	0.81	1.19	0.42	3.35	1.31	4167	4607	6.30	43.7	b.d.l.	0.58	b.d.l.	9.41
	C1-03	1084	10477	6.60	224	10.8	0.13	0.00	370	1.66	11.3	0.51	0.02	0.44	340	0.29	2.34	0.86	2520	4817	2.48	38.9	b.d.l.	1.16	b.d.l.	8.32
	C1-04	1964	11216	4.09	63.6	6.93	0.21	0.01	945	1.70	13.0	0.80	0.01	0.87	2.01	0.60	5.00	1.77	5265	4190	6.34	50.9	0.55	1.54	b.d.l.	9.31
	C1-05	1579	10781	4.38	117	8.64	0.45	b.d.l.	606	3.34	16.2	0.61	0.00	0.57	4.31	0.47	1.32	1.55	5551	3669	5.86	268	0.27	0.31	1.09	10.6
	C1-06	1533	9600	6.77	206	5.60	0.23	0.07	672	1.87	13.9	0.56	0.00	0.49	4.04	0.41	1.65	1.25	4219	4279	11.2	34.0	0.15	1.15	0.68	10.0
	C2-01	1472	7993	4.83	210	40.5	0.17	0.01	704	2.81	15.2	0.41	0.00	0.38	8.07	0.70	1.19	1.32	8403	3374	3.47	35.3	b.d.l.	0.40	2.54	7.69
	C2-02	1577	10137	4.16	252	8.61	0.35	b.d.l.	728	3.11	15.0	0.26	0.00	0.45	2.37	0.63	2.75	1.56	5317	2988	4.05	37.4	0.61	0.39	1.94	7.08
	C2-03	2670	12392	6.08	615	16.1	0.50	0.01	1523	1.07	14.1	0.56	0.02	1.01	7.96	0.41	2.96	1.18	4040	5717	3.43	44.5	0.78	0.68	5.91	6.72
	C2-04	2140	6805	1.91	51.2	14.4	0.29	0.01	782	5.27	8.74	0.23	0.00	0.31	b.d.l.	0.36	1.21	2.19	3489	1439	3.18	22.1	0.73	0.59	b.d.l.	7.23
	C2-05	1882	8269	2.98	270	9.61	0.28	0.03	695	3.84	19.0	0.15	0.00	0.29	1.38	0.35	3.24	1.84	3079	2037	3.99	19.3	b.d.l.	0.26	0.58	5.92
	C2-06	2079	6159	2.53	150	10.7	0.21	b.d.l.	1000	2.92	8.89	0.26	b.d.l.	0.33	b.d.l.	0.36	0.88	2.07	2864	2159	2.68	25.8	b.d.l.	0.17	3.81	5.78
	C2-07	2230	6407	3.94	216	11.2	0.29	0.01	1122	4.29	18.2	0.53	0.00	0.41	1.36	0.49	1.42	2.09	4290	2517	2.77	28.7	0.17	0.71	b.d.l.	5.55
	C2-08	2091	7975	6.72	393	4.11	0.20	0.01	660	2.70	16.0	0.50	0.00	0.42	b.d.l.	0.33	1.24	1.14	4081	3974	2.32	204.1	b.d.l.	0.79	b.d.l.	8.65
YLL14-37-2	C1-01	2044	10106	2.75	128	7.00	0.30	0.00	1266	0.76	36.6	0.65	0.00	0.59	117	0.76	4.04	1.45	7138	4238	3.43	45.0	0.24	1.23	b.d.l.	8.65
	C1-02	725	13789	4.46	327	5.52	0.40	0.01	481	b.d.l.	16.9	0.61	b.d.l.	0.43	10.9	0.20	2.38	0.71	2749	6061	0.50	29.1	0.43	0.25	b.d.l.	9.94
	C1-03	1612	7255	1.39	29.5	14.0	0.37	0.01	714	0.91	22.7	0.46	0.01	0.50	b.d.l.	0.53	1.73	0.93	4590	2381	2.84	34.1	b.d.l.	0.41	1.93	7.11
	C2-01	1251	5175	3.11	83.0	41.8	0.31	0.00	628	0.81	24.8	1.14	0.00	0.54	b.d.l.	0.81	2.42	1.41	7790	3116	5.15	24.9	b.d.l.	0.74	b.d.l.	10.7
	C2-02	722	6176	4.29	103	5.51	0.80	b.d.l.	317	0.27	18.3	1.11	b.d.l.	0.47	b.d.l.	0.77	4.66	0.73	7264	4912	1.97	34.1	0.29	0.94	b.d.l.	13.4
	C2-03	1447	6723	2.99	42.7	8.11	1.55	0.01	856	1.21	26.3	1.19	0.16	0.72	8.41	1.27	3.35	1.56	10891	3379	8.80	61.5	0.34	0.31	1.10	13.4
	C2-04	b.d.l.	9554	2.42	34.0	30.0	0.38	b.d.l.	387	0.38	18.6	0.84	0.00	0.30	6.47	1.00	3.50	0.72	13649	6837	0.49	34.6	0.31	0.41	b.d.l.	12.6

Note: b.d.l., below detection limit.
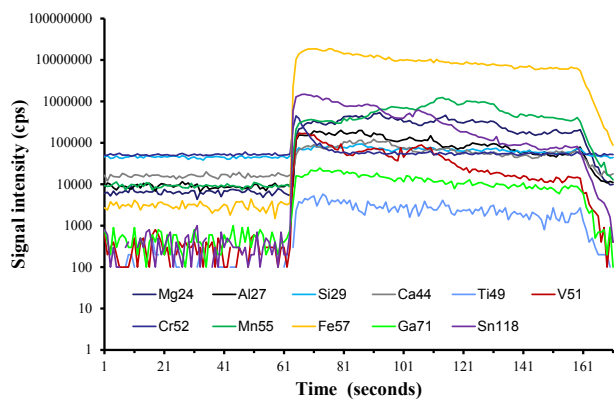
Fig. 8. Representative single-spot LA–ICP–MS spectra for selected elements in magnetite from sample KD14-17.

by hydrothermal fluids. We infer that the two types of magnetite formed in different stages of hydrothermal activity, and that the later Type B magnetites experienced greater degree of wall-rock alteration (see Hu et al. 2014 and references therein).

Elements commonly substituting into the spinel group minerals, such as Fe, Al, Ti, Mg, Mn, Zn, Cr, V, Ni, Co, and Ga, are commonly referred to as 'spinel elements' (Dare et al., 2014). The composition of magnetite, as a member of the spinel group minerals, is a function of temperature, cooling rate, redox reactions (e.g., oxygen fugacity or fO_2), and silica activity, amongst other factors (Buddington and Lindsley, 1964; Ray and Webster, 2007; Nadoll et al, 2012; Nadoll et al., 2014; Huang et al., 2013, 2014, 2015; Dare et al., 2014). As a result, these 'spinel elements' are regarded as useful indicators for potentially distinguishing magnetites from different sources (Rusk et al., 2009). The Ti, V, Al, Mn, and Ga contents can potentially be used for distinguishing low- and high-temperature mineral systems (Nadoll et al., 2014). However, other factors, such as fO_2 and re-equilibration processes related to late hydrothermal fluids, can also exert a marked influence on cation substitution, and thereby may mask other process-related compositional trends (Nadoll et al., 2014).

The oxygen fugacity of hydrothermal fluids can govern element behavior, and may influence the segregation of ore-forming metals (e.g., Au and Ag) during the ore forming process (Li et al., 2018). For example, Vanadium is an immobile element during DRP, and its oxidation state in different fugacity ranges can lead to occurrence of V ions in the V^{3+}, V^{4+}, or V^{5+} states. Vanadium is usually incorporated preferentially into magnetite structure in the V^{3+} states at low oxygen fugacity (Nadoll et al., 2014). Consequently, the oxidation state of V can be used to estimate the relative fO_2 prevalent during the ore-forming process (Acosta-Góngora et al., 2014; Nadoll et al., 2014). Likewise, silicate melt experiments have demonstrated that the fractionation of V into magnetite is a function of fO_2 (Righter et al., 2006).

Furthermore, magnetite is now considered more susceptible to hydrothermal alteration/replacement than previously thought (Hu et al., 2014, 2015; Huang et al., 2019). Silicon, Mg, Ca, Mn and Al behave as mobile elements, whereas Ti and V are relatively immobile during these processes (Hu et al., 2015). For these reasons, the relatively immobile elements Ti and V were used to investigate the original hydrothermal environment of magnetite formation in the LSKD.

Magnetites from the LSKD contain low amounts of Ti + V and variable proportions of Al + Mn, compared with typical magnetites from other types of deposits (Fig. 10a). In addition, Type A magnetites have higher contents of Ti and V, and lower contents of Al + Mn compared with Type B magnetites, and in detail Type B1 magnetites have much lower contents of V compared with Type B2 magnetites (Figs. 9a, e, and 10a). Previous research has shown that magnetites formed at high temperature and/or relatively reducing conditions commonly exhibit

oxy-exsolution of Ti-rich oxides in response to subsequently increasing fO_2 and decreasing temperature, which leads to the low-Ti content in magnetite (Ray and Webster, 2007). However, the exsolution features are absent in hydrothermal low-Ti magnetite owing to the limited solubility of Ti in most hydrothermal fluids (e.g., Van Baalen, 1993). Our detailed microscopic observations reveal that both types of magnetite from the LSKD lack evidence of exsolution lamellae and associated porosity. Hence, the low Ti and V contents in these magnetites are interpreted to have resulted from low-temperature conditions of hydrothermal activity. This is in agreement with the low-temperature fluid inclusions results in this deposit (Lei et al., 2012; Meng et al., 2009). Lei et al. (2012) studied individual fluid inclusions (mainly two-phase inclusions) contained in quartz, and reported homogenization temperatures in the range of 140–340 °C (mean = 208 °C). Meng et al. (2009) reported homogenization temperatures in the range of 101–400 °C (mostly between 110 and 220 °C) for vein quartz, and 120–280 °C (mostly between 110 and 240 °C) for calcite. Type A magnetites identified in this study formed prior to the main-stage sulphides, implying that the early barren hydrothermal fluid was relatively high temperature. In contrast, Type B magnetites formed later, in association with the early (stage 1) and main mineralization (stage 2) stages, indicating that the late ore-forming hydrothermal fluid was lower temperature. The widespread distribution of trace elements in the later Type B magnetites also indicate that these magnetites underwent a greater degree of alteration than early Type A magnetites, supporting the idea that the fluid of the main mineralization stage was more pervasive and intense in its effect compared with the early fluid.

The results of this study are obviously different from the composition characteristics of magnetite occurring in other deposit types, including porphyry Cu, skarn, IOCG and Kiruna (IOA) deposits (Fig. 10a). Nevertheless, its composition follows an overall decreasing trend of temperature (Fig. 10a). Our study confirms that magnetites not only could be developed in low-temperature hydrothermal Ag–Pb–Zn deposits, and their composition also can effectively trace the mineralization process. Together with the inferred genetic characteristics of the low-temperature hydrothermal fluid forming magnetite in the LSKD, this study informs research into magnetite genesis in various types of deposit around the world, and indicates a viable proposed extension of the boundary between magmatic magnetite and hydrothermal magnetite (red line in Fig. 10b), based on the results of this study. However, more data will be required in the future.

7.2. Constraints on hydrothermal fluid evolutions

Magnetite can be used as an indicator mineral for hydrothermal alteration and mineralization processes (Angerer et al., 2012). Properties of hydrothermal fluids, including temperature, salinity, composition (e.g., F^- and Cl^- contents) and fluid fO_2, along with the types of alteration mineral produced and the wall rocks alteration, are all important factors in the dissolution of primary magnetite (e.g., Whitney et al., 1985; Hemley and Hunt, 1992; Hu et al., 2015). The contrasting trace element compositions of the two types of magnetite present in the LSKD also help to better understand the characteristics of hydrothermal fluids in the early and late stages, and provide insights into the formation of Ag–Pb–Zn mineralization. However, the alteration of wall rocks, as well as DRP may significantly obscure the original characteristics of initial hydrothermal mineral precipitation (Putnis, 2009; Altree-Williams et al., 2015). Nevertheless, the proportions of mobile elements (e.g., Mg, Mn, Sn, Ga, and Mo) in magnetites are sensitive to alteration and DRP, and can be used to constrain the evolution of hydrothermal fluids and identify the key controls on mineralization.

7.2.1. Effects of temperature

Previous studies have shown that increasing temperature can enhance iron solubility, and consequently induce iron undersaturation in fluid, leading to dissolution of primary magnetite and formation of
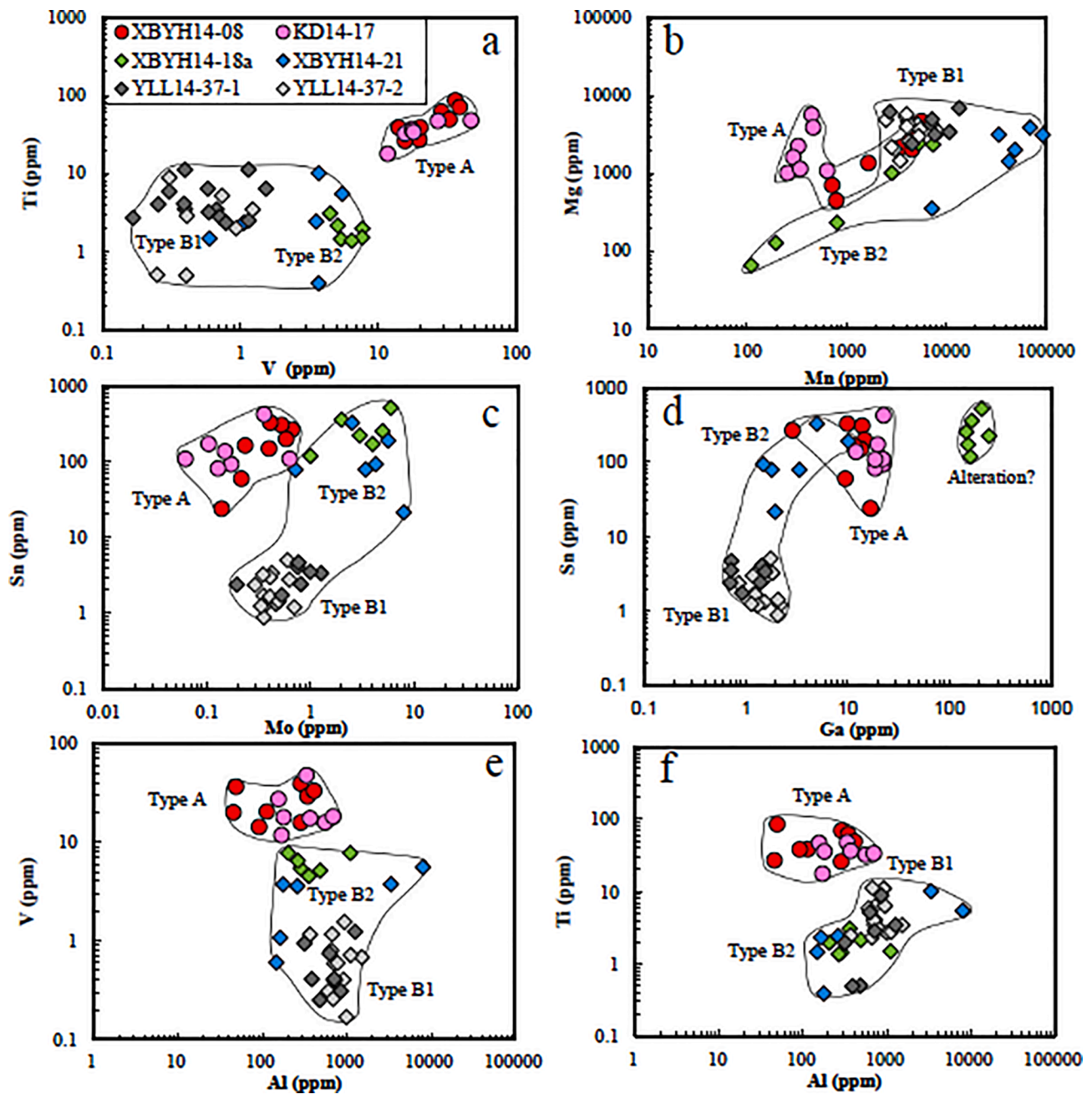
Fig. 9. Scatter plots for a selection of relevant spinel elements in magnetite from the LSKD. (a) Ti-V, (b) Mg-Mn, (c) Sn-Mo, (d) Sn-Ga, (e) V-Al and (f) Ti-Al.

secondary varieties during subsequent decreasing temperatures (e,g Hemley and Hunt, 1992; Hu et al., 2014; Chen et al., 2020). As noted above, both types (A and B) of magnetite were formed under relatively low-temperature conditions, and evolution of the hydrothermal fluid was most likely a process of cooling over time (Lei et al., 2012; Meng et al., 2009). Decreasing temperature is thought to be an important control on metal precipitation (Meng et al., 2009), rather than an influence on DRP. Furthermore, the temperature range inferred for the LSKD hydrothermal fluids (110–240 °C) is not high enough for the dissolution of primary magnetite (Lei et al., 2012; Meng et al., 2009). This is consistent with the occurrence of vein and veinlet in granite porphyry (Fig. 5g), in which fine vein/veinlet ores developed in a rapidly cooling environment as hydrothermal fluids entered wall rocks along open fractures. Compared with the positive relationship between Ti and V (Fig. 9a), negative relationships for V versus Al and Ti versus Al (Fig. 9e, f), indicate that other controlling factors could have affected

trace element contents in magnetite from the LSKD. Although fO_2 is generally recognized as an important control on trace element contents in magnetite, V content variation in the different types of LSKD magnetite does not show relationship with fO_2 and can be explained by temperature alone. Until further reliable evidence is obtained, we consider the effect of hydrothermal fluid fO_2 on magnetite trace element content variation negligible.

7.2.2. Effect of alteration

Type B2 magnetites exhibit higher Ga, Mo, and Sn contents than their contents from other magnetite types (Fig. 9). These features are inconsistent with the low contents of V and Ti in Type B2 samples, which are considered to be related to cooling over time. Thus, other factors that control trace element contents in magnetites should be considered. In addition to the influence of temperature, wall-rock alteration may play an important role in producing the wide variation observed in Ga, Mo,
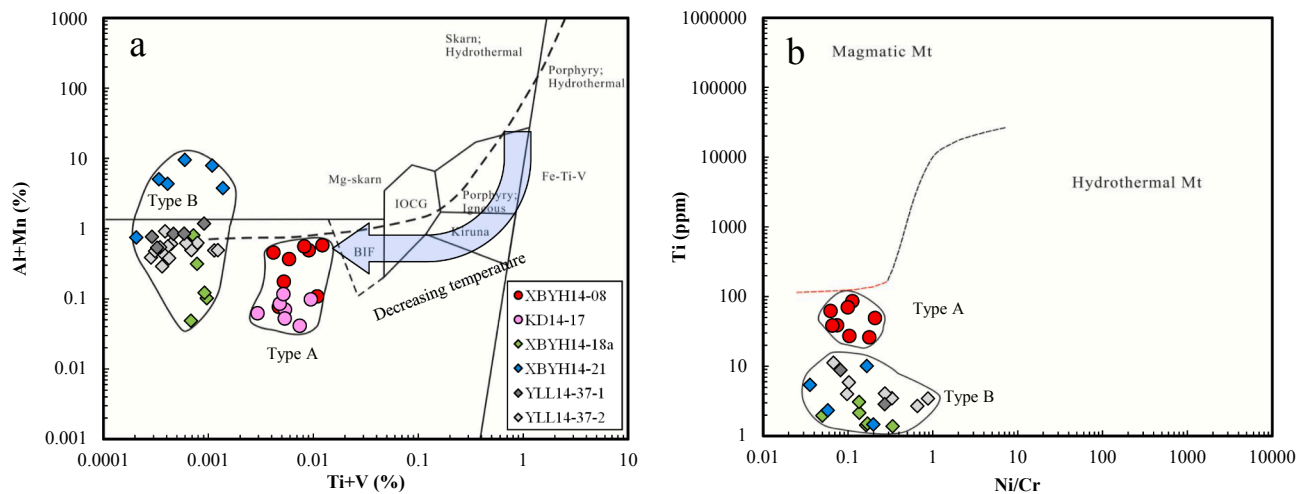
Fig. 10. Al + Mn vs. Ti + V and Ti vs. Ni/Cr diagrams for magnetite from the LSKD. Reference fields are modified from Nadoll et al. (2014) and Dare et al. (2014). The arrow in (a) indicates the direction of temperature reduction, and the dashed red line in (b) indicates a viable proposed extension of the boundary between magmatic magnetite and hydrothermal magnetite. Deposit type abbreviations: IOCG = iron oxide copper–gold deposits, Kiruna = Kiruna-type magnetite-apatite deposits. (For interpretation of the references to colour in this figure legend, the reader is referred to the web version of this article.)

and Sn contents. Bhattacharya et al. (2007) studied hydrothermal alteration of metamorphic magnetite from the Neo Dala banded iron formation, in the Archean Iron Ore Group, India, by analyzing magnetite chemistry. Those authors suggested that elevated Mo and Sn contents could be attributed to hydrothermal metasomatism associated with granitic host rocks. Furthermore, Nadoll et al. (2014) reported that hydrothermal magnetites from a magnesian skarn exhibited consistently higher Sn and Ga than those from other settings. However, there is no skarn present in the LSKD based on the known ore deposit geology. Therefore, it is unreasonable to consider the high Sn and Ga contents in magnetites from the LSKD to be a result of skarnization. Rather, the most likely cause of the high levels of Ga, Mo, and Sn in the LSKD magnetites is inheritance from hydrothermal alteration of wall rock. It is noted that samples XBYH14-18a and -21 underwent a higher degree of alteration (e.g., chloritization) compared with samples YLL14-37-1 and -2 (Fig. 5g). The latter two samples display distinct boundaries contacting granite porphyry wall rock, indicating their relatively low degree of alteration. A previous study has shown that the chemical behavior of Ga is closely related to the concentration of Al in the hydrothermal system (Liu et al., 1984). In addition, sample XBYH14-18a reveals obvious wall-rock alteration (chloritization), wherein Al is the major component (Liu et al., 1984). Therefore, it is inferred that the high Ga content in LSKD magnetites is most likely the result of chloritization.

Small particles of cassiterite were found within siderite coexisting with Type A magnetite, indicating that the early hydrothermal fluid contained significant Sn. It therefore seems likely that the high Sn contents of the Type A magnetites were derived from high-Sn-bearing early hydrothermal fluid.

7.3. Implications for Ag migration and deposition

As discussed before, multi-stage hydrothermal fluid influx produced the base and Ag mineralization through a cooling process and later, a more pronounced alteration in the LSKD. Therefore, the evolution of hydrothermal fluids deduced from trace elements of magnetite can provide meaningful insights into the mechanism of Ag–Pb–Zn migration and precipitation in the LSKD.

Williams-Jones and Migdisov (2014) suggested that Ag occurs predominantly as Ag^+ in hydrothermal fluids, similar to Au. The transport speciation of Ag is dominated by bisulphide and chloride species, and is affected by the temperature, pH, and redox conditions of hydrothermal fluids (Stefansson and Seward, 2003; Shang et al., 2003, 2004). Previous

experimental studies have demonstrated that Ag chloride species ($AgCl^{2-}$) are dominant under relatively high temperatures (>400 °C) and/or acidic to neutral conditions, whereas Ag bisulphide species ($AgHS^0$) predominate at lower temperatures (<200 °C), and/or near-neutral to basic conditions, and relatively low oxygen fugacity (e.g., Seward, 1976; Gammons and Barnes, 1989; Gammons and Williams-Jones, 1995; Stefansson and Seward, 2003).

Carbonate minerals in the LSKD show a sequence from siderite through Fe- and Mn-rich carbonate minerals, to Mn-rich carbonate minerals over time. These features indicate that the later fluids contained much higher Mn contents compared with the early fluids. The element Mn can be successively enriched in hydrothermal fluids during fluid–rock interactions, and where the fluid is Cl^- rich (Hu et al., 2014, 2015; Nadoll et al., 2010). Zhong et al. (2015a) argued that the concentration of Cl^- would predominate over that of reduced sulfur by several orders of magnitude, and consequentially Cu, Pb, and Zn are transported mainly with chloride complexes at low temperature. Furthermore, increasing salinity, especially the Cl^- content in ore-forming fluids, can also enhance Fe solubility, thereby leading to disequilibrium between precipitated magnetites and late influxes of hydrothermal fluid (Hu et al., 2014).

Meng et al. (2007a) established that ore-forming hydrothermal fluids in the LSKD were a medium to highly saline, $CaSO_4/MgCl_2$–NaCl–KCl–H_2O-bearing solution system enriched in halogens and alkali elements. In the early stage, hydrothermal fluids were characterized by relatively high temperatures (420–300 °C, Zuo et al., 2009) and acidity (pH = 4.9; Meng et al., 2007a). These characteristics suggest that Ag–, Pb– and Zn–Cl complexes constituted the main transport phases. Thus, Cl-complexes were likely the dominant fluid species involved in metal ion transport in the LSKD system.

Controls on mineral precipitation include decreasing fluid temperature, change in fluid pH (e.g., increasing pH for chloride species, or decreasing pH for bisulphide species formation), and change in fO_2 (e.g., decreasing fO_2 for chloride species), or some combination of these (Akinfiev and Zotov, 2001; Shang et al., 2003, 2004; Liu et al., 2012; Zhong et al., 2015). In the studied samples, Ag sulphide (acanthite), the most common Ag mineral in the LSKD, is distributed in association with other sulphides in veinlets around relatively early-formed pyrite and galena (Fig. 7). The occurrence of Ag-bearing minerals in microcleavage indicates the influence of extensional fracturing in and around early-formed sulphides at sites of later Ag precipitation. While ore-forming fluids pass through wall rocks rich in reduced S, the lower

stability of Ag–Cl complexes compared with those of Pb–Cl and Zn–Cl complexes should result in preferential precipitation of Ag sulphide from a Cl-rich fluid system (Shang et al., 2003, 2004). Large amounts of relatively early-formed sulphides of Fe, Pb and Zn as S-bearing reductive minerals are found in porphyry- and stratabound-type orebodies in the LSKD. Simple estimates based on Ag, Pb and Zn reserves from the LSKD show that the reduced sulfur in sulphides can supply sufficient S^{2-} directly, whereas carbonates can neutralize metal-bearing acid sulphide fluids, thereby precipitating Ag from Ag-Cl fluid complexes. Furthermore, reduction of Fe^{2+} and Mn^{2+} in Fe–Mn-bearing carbonates could further reduce Ag sulphide to native silver (Lu et al., 2012).

It is therefore likely that Ag–Cl complexes constituted the main Ag transport phase, with the dissolution of earlier-formed sulphides of Fe, Pb, and Zn supplying reduced S for the final precipitation of Ag in the LSKD. These inferences indicate that Ag transportation by Ag–Cl complexes in hydrothermal fluid and precipitation with reduced S supplied by dissolution of early-formed sulphide and/or acid-neutralization by carbonate minerals, led to Ag ore formation.

8. Conclusions

Results of magnetite LA–ICP–MS analyses coupled with detailed microscopic observation of Ag–Pb–Zn ores from the Lengshuikeng deposit (LSKD) allow the following conclusions to be drawn. Two types of magnetite were distinguished from representative samples collected from the LSKD. Type A magnetites are large, show euhedral and inclusion-free forms, and coexist with siderite, having formed prior to the surrounding sulphides. Type B magnetites are smaller, display irregular and anhedral forms occurring as alteration features, and coexist with sulphides and Fe–Mn-bearing carbonate minerals. Both types of magnetite appear to have formed from the ingress of generations of relatively low-temperature hydrothermal fluids containing small amounts of Ti and V. Type A magnetites formed early from somewhat higher-temperature (>240 °C) fluids that contained relatively small amounts of ore-forming components. Type B magnetites were formed during the early (B1, stage 1) as well as the main mineralization (B2, stage 2) stages under alteration, dissolution and reprecipitation processes from late ore-forming hydrothermal fluids. The late hydrothermal fluids were relatively low-temperature (<240 °C), rich in Cl^- and Mn. The inferred characteristics of late hydrothermal fluids together with detailed microscopic observations suggest that metal–Cl complexes were the main migration phases of Ag, Pb, and Zn in the LSKD, and that interaction with early-formed Fe, Pb, and Zn sulphides supplied the required reduced S for the final precipitation of Ag sulphides.

Declaration of Competing Interest

The authors declare that they have no known competing financial interests or personal relationships that could have appeared to influence the work reported in this paper.

Acknowledgments

References

Acosta-Góngora, P., Gleeson, S.A., Samson, I.M., Ootes, L., Corriveau, L., 2014. Trace element geochemistry of magnetite and its relationship to Cu-Bi-Co-Au-Ag-U-W mineralization in the great bear magmatic zone, NWT Canada. Econ. Geol. 109, 1901–1928.

Akinfiev, N.N., Zotov, A.V., 2001. Thermodynamic description of chloride, hydrosulfide, and hydroxo complexes of Ag(I), Cu(I), and Au(I) at temperatures of 25–500 °C and pressures of 1–2000 bar. Geochem. Int. 39, 990–1006.

Altree-Williams, A., Pring, A., Ngothai, Y., Brugger, J., 2015. Textural and compositional complexities resulting from coupled dissolution–reprecipitation reactions in geomaterials. Earth-Sci. Rev. 150, 628–651.

Angerer, T., Hagemann, S.G., Danyushevsky, L., 2012. Geochemical evolutions of the banded iron formation-hosted high-grade iron ore system in the Koolyanobbing Greenstone Belt, Western Australia. Econ. Geol. 107, 599–644.

Barnes, S.J., Maier, W.D., Ashwal, L.D., 2004. Platinum-group element distribution in the Main Zone and Upper Zone of the Bushveld Complex, South Africa. Chem. Geol. 208, 293–317.

Beaudoin, G., Dupuis, C., 2009. Iron-oxide trace element fingerprinting of mineral deposit types. In: Corriveau, L., Mumin, H. (Eds.), Exploring for Iron Oxide Copper–Gold Deposits: Canada and Global Analogues, Short Course Volume. Geological Association of Canada Annual Meeting, pp. 107–121.

Bhattacharya, H.N., Chakrabort, I., Ghosh, K.K., 2007. Geochemistry of some banded iron-formations of the Archean supracrustals, Jharkhand-Orissa region, India. J. Earth Syste. Sci. 116, 245–259.

Buddington, A., Lindsley, D., 1964. Iron-titanium oxide minerals and synthetic equivalents. J. Petrol. 5, 310–357.

Carew, M.J., 2004. Controls on Cu–Au Mineralisation and Fe-oxide metasomatism in the Eastern Fold Belt, NW Queensland, Australia. PhD. James Cook University, Townsville.

Chen, F., Deng, J., Wang, Q.F., Huizenga, J.M., Li, G.J., Gu, Y.W., 2020. LA-ICP-MS trace element analysis of magnetite and pyrite from the Hetaoping Fe-Zn-Pb skarn deposit in Baoshan block, SW China: implications for ore-forming processes. Ore Geol. Rev. 117.

Chen, G.D., 2006. Thinking and suggestion for mineral resources perambulation in main metallogenic belt in east China. Resour. Surv. Environ. 27 (4), 251–254 (in Chinese).

Chen, W.T., Zhou, M.F., Gao, J.F., Hu, R.Z., 2015. Geochemistry of magnetite from Proterozoic Fe-Cu deposits in the Kangdian metallogenic province,, SW China. Mineral. Deposita 50, 795–809.

Chen, W.T., Zhou, M.F., Li, X., Gao, J.F., Hou, K., 2015. In-situ LAICP-MS trace elemental analyses of magnetite: Cu-(Au, Fe) deposits in the Khetri copper belt in Rajasthan province, NW India. Ore Geol. Rev. 65, 929–939.

Dare, S.A., Barnes, S.J., Beaudoin, G., Méric, J., Boutroy, E., PotvinDoucet, C., 2014. Trace elements in magnetite as petrogenetic indicators. Mineral. Deposita 49, 785–796.

Dare, S.A.S., Barnes, S.J., Beaudoin, G., 2012. Variation in trace element content of magnetite crystallized from a fractionating sulfde liquid, Sudbury, Canada: implications for provenance discrimination. Geochim. Cosmochim. Acta 88, 27–50.

Deng, S.M., 1991. Cryptoexplosive breccia dyke in the paleovolcanic rock zone in Lengshuikeng, Guixi, Jiangxi Province and its metallogeny. Geol. Sci. Technol. Jiangxi 18, 28–32 (in Chinese).

Ding, X., Jiang, S.Y., Ni, P., Gu, L.X., Jiang, Y.H., 2005. Zircon SIMS U-Pb geochronology of host granitoids in Wushan and Yongping copper deposits, Jiangxi Province. Geol. J. China Univ. 11 (3), 383–389 (in Chinese).

Dupuis, C., Beaudoin, G., 2011. Discriminant diagrams for iron oxide trace element fingerprinting of mineral deposit types. Miner. Deposita 46, 319–335.

Gammons, C.H., Barnes, H.L., 1989. The solubility of Ag2S in near-neutral aqueous sulfide solutions at 25 to 300 °C. Geochim. Cosmochim. Acta 53 (2), 279–290.

Gammons, C.H., Williams-Jones, A.E., 1995. Hydrothermal geochemistry of electrum; thermodynamic constraints. Econ. Geol. 90 (2), 420–432.

Hemley, J.J., Hunt, J.P., 1992. Hydrothermal ore-forming processes in the light of studies in rock-buffered systems; II. Some general geologic applications. Econ. Geol. 87, 23–43.

Hu, H., Lentz, D., Li, J.W., McCarron, T., Zhao, X.F., Hall, D., 2015. Reequilibration processes in magnetite from iron skarn deposits. Econ. Geol. 110, 1–8.

Hu, H., Li, J.W., Lentz, D., Ren, Z., Zhao, X.F., Deng, X.D., Hall, D., 2014. Dissolution-reprecipitation process of magnetite from the Chengchao iron deposit: Insights into ore genesis and implication for in-situ chemical analysis of magnetite. Ore Geol. Rev. 57, 393–405.

Huang, X.W., Gao, J.F., Qi, L., Zhou, M.F., 2015. -situ LA-ICPMS trace elemental analyses of magnetite and Re-Os dating of pyrite: The Tianhu hydrothermally remobilized sedimentary Fe deposit, NW China. Ore Geol. Rev. 65, 900–916.

Huang, X.W., Qi, L., Meng, Y.M., 2014. Trace element geochemistry of magnetite from the Fe(-Cu) deposits in the Hami region Eastern Tianshan orogenic belt, NW China. Acta Geol. Sinica 88, 176–195.

Huang, X.W., Sappin, A.A., Boutroy, É., Beaudoin, G., Makvandi, S., 2019. Trace element composition of igneous and hydrothermal magnetite from porphyry deposits: relationship to deposit subtypes and magmatic affinity. Econ. Geol. 114, 917–952.

Huang, X.W., Zhou, M.F., Qi, L., Gao, J.F., Wang, Y.W., 2013. Re-Os isotopic ages of pyrite and chemical composition of magnetite from the Cihai magmatic-hydrothermal Fe deposit, NW China. Mineral. Deposita 48, 925–946.

JXBGMR (Bureau of Geology and Mineral Resources of Jiangxi Province),, 1984. In: Regional Geology of the Jiangxi Province. Geological Publishing House, Beijing, pp. 1–921 (in Chinese).

JXBGMR (Department of Geology and Mineral Resources of Jiangxi Province), 1997. In: Stratigraphy (Lithostratic) of Jiangxi Province. China University of Geosciences Press, Wuhan, pp. 9–50 (in Chinese).

Leach, D.L., Sangster, D.F., Kelley, K.D., Large, R.R., Garven, G., Allen, C.R., Gutzmer, J., Walters, S., 2005. Sediment-hosted lead-zinc deposits: a global perspective. In: Hedenquist, J.W., Thompson, J.F.H., Goldfarb, R.J., Richards, J.P. (Eds.), One Hundredth Anniversary Volume. Society of Economic Geologists, pp. 561–607.

Lei, Y., Starostin, V.I., Prokof'ev, V.Y., Gango, U., 2012. Stratiform ore of the large Lengshuikeng silver deposit, China: Mineralogy, fluid inclusions, stable O and C isotopes. Geolol.. Ore Deposits 54, 219–232.

Leng, C.B., Qi, Y.Q., 2018. The genesis of Lengshuikeng Ag-Pb-Zn Orefield: constrains from in-situ LA-ICPMS analyses of minor and trace elements for sphalerite and Galena. Acta Geol. Sin. 91 (10), 2256–2272 (in Chinese).

Li, D.F., Fu, Y., Sun, X.M., Hollings, P., Liao, J.L., Liu, Q.F., Feng, Y.Z., Liu, Y., Lai, C.K., 2018. LA-ICP-MS trace element mapping: Element mobility of hydrothermal magnetite from the giant Beiya Fe-Au skarn deposit, SW China. Ore Geol. Rev. 92, 463–474.

Li, W.X., Li, X.H., Li, Z.X., Lou, F.S., 2008. Obduction-type granites within the NE Jiangxi Ophiolite: implications for the final amalgamation between the Yangtze and Cathaysia Blocks. Gondwana Res. 13, 288–301.

Li, Q., Jiang, S., 2016. Trace and rare earth element characteristics in Fe-Mn carbonates associated with stratiform Ag-Pb-Zn mineralization from the Lengshuikeng ore district, Jiangxi Province: implications for their genesis and depositional environment. J. Earth Sci. 27, 571–583.

Li, Z.K., Li, J.W., Chen, L., Zhang, S.X., Zheng, S., 2010a. Occurrence of silver in the Shagou Ag-Pb-Zn Deposit, Luoning County, Henan Province: implication for mechanism of silver enrichment earth science. J. China Univ. Geosci. 35 (4), 621–636 (in Chinese).

Li, Z.X., Zhang, L., Powell, C.M., 1996. Positions of the East Asian cratons in the Neopreterozoic supercontinent Rodinia. Aust. J. Earth Sci. 43, 593–604.

Li, Z.X., Li, X.H., Wartho, J.A., Clark, C., Li, W.X., Zhang, C.L., Bao, C., 2010b. Magmatic andmetamorphic events during the Early PaleozoicWuyi-Yunkai Orogeny, southeastern South China: new age constraints and P-T conditions. Geol. Soc. Am. Bull. 122, 772–793.

Liu, X., Lu, X., Wang, R., Zhou, H., 2012. Silver speciation in chloride-containing hydrothermal solutions from first principles molecular dynamics simulations. Chem. Geol. 294–295, 103–112.

Liu, X., Sun, Z.M., Ma, Y.S., 1994. In: Ore-controlling Structure and Ore-forming Prediction in North Wuyishan and Surrounding area. Seismological Publishing House, Beijing, pp. 1–192 (in Chinese).

Liu, Y.J., Cao, L.M., Li, Z.L., Wang, H.N., Chu, T.Q., Zhang, J.R., 1984. In: Element Geochemistry. Science Press, Beijing, pp. 1–548 (in Chinese).

Lu, H.J., Hua, R.M., Mao, G.Z., Long, G.M., 2007. Isotope geochronological study of igneous rocks in Northeastern Jiangxi Province and its implication to geologic evolution. Geol. Rev. 53, 207–216.

Lu, R., Mao, J.W., Gao, J.J., Su, H.M., Zheng, J.H., 2012. Geological characteristics and occurrence of silver in Xiabao Ag-Pb-Zn deposit, Lengshuikeng ore field, Jiangxi Province, east China. Acta Petrol. Sinica 28 (1), 105–121 (in Chinese).

Luo, P., Wu, G.G., Zhang, D., Di, Y.J., Wang, C.M., Wang, Y.Q., 2009. Geochemistry and genesis of Shengmikeng lead–zinc deposit in northern Wuyi, Eastern China. 15: 349–362 (in Chinese).

Mao, J.W., Cheng, Y.B., Chen, M.H., Franco, P., 2013. Major types and time–space distribution of Mesozoic ore deposits in south China and their geodynamic settings. Miner. Deposita 48, 267–294.

Mei, Y.W., 1998. The Wuyishan orogen and its ore-forming process. Jiangxi Geol. 12 (2), 109–115.

Meng, X.J., Dong, G.Y., Liu, J.G., 2007a. In: Lengshuikeng Porphyry Pb–Zn–Ag Deposit in Jiangxi Province. Geological Publishing House, Beijing, pp. 1–184 (in Chinese).

Meng, X.J., Hou, Z.Q., Dong, G.Y., Liu, J.G., Qu, W.J., Yang, Z.S., Zou, L.Y., Wan, L.J., Xiao, M.Z., 2007b. The geological characteristics and Re–Os isotope age of molybdenite of the Xiongjiashan molybdenum deposit, Jiangxi Province. Acta Geol. Sinica 81 (7), 946–951 (in Chinese).

Meng, X.J., Hou, Z.Q., Dong, G.Y., Liu, J.G., Zuo, L.Y., Yang, Z.S., Xiao, M.Z., 2009. Geological characteristics and mineralization timing of the Lengshuikeng Porphyry Pb-Zn-Ag deposit, Jiangxi Province. Acta Geol. Sinica 83 (12), 1951–1967.

Meng, X.J., Xu, W.Y., Yang, Z.S., Hou, Z.Q., Li, Z.Q., Yu, Y.S., Xiao, M.Z., He, X.R., Wan, H.Z., 2012. Time limit of volcanic-magmatic action in Lengshuikeng orefield, Jiangxi: Evidence from SHRIMP zircon U-Pb ages. Miner. Deposits 31 (4), 831–838 (in Chinese).

Nadoll, P., Angerer, T., Mauk, J.L., French, D., Walshe, J., 2014. The chemistry of hydrothermal magnetite: a review. Ore Geol. Rev. 61, 1–32.

Nadoll, P., Mauk, J.L., Hayes, T.S., Koenig, A.E., Box, S.E., 2012. Geochemistry of magnetite from hydrothermal ore deposits and host rocks of the Mesoproterozoic Belt Supergroup, United States. Econ. Geol. 107, 1275–1292.

Nadoll, P., Mauk, J.L., Leveille, R., Koenig, A.E., 2010. Geochemistry of magnetite from Cu–Mo porphyry + skarn, and Climax Mo deposits in the western United States. In: PálMolnár, E. (Ed.), IMA 2010. Department of Mineralogy, Geochemistry and Petrology. University of Szeged, Budapest, pp. 1–507.

No. 912, No. 912 Geological Team of Geology and Mineral Resources Exploration Development Bureau of Jiangxi Province, 1997. Geology report on the Lengshuikeng Ag deposit, Guixi County, Jiangxi Province. Jiangxi Bureau of Geology and Mineral Exploration and Development, Nanchang, pp. 1–53.

Putnis, A., 2009. Mineral replacement reactions. Rev. Mineral. Geochem. 70, 87–124.

Ray, G.E., Webster, I., 2007. Geology and chemistry of the low Ti magnetite-bearing Heff Cu-Au Skarn and its associated plutonic rocks, Heffley Lake, South-Central British Columbia. Explor. Min. Geol. 16 (3–4), 159–186.

Qi, Y.Q., Hu, R.Z., Li, X.F., Leng, C.B., Liu, S., Wu, L.Y., Liu, R., 2015. Mineral chemical characteristics of sphalerite and genetic constraints of iron and manganese carbonate in Lengshuikeng Ag-Pb-Zn ore deposit, Jiangxi Province, China. Acta Mineral. Sinica 35 (2), 136–146 (in Chinese).

Qi, Y.Q., Hu, R.Z., Liu, S., Coulson, I.M., Qi, H.W., Tian, J.J., Zhu, J.J., 2016. Petrogenesis and geodynamic setting of Early Cretaceous mafic-ultramafic intrusions, South China: a case study from the Gan-Hang tectonic belt. Lithos 258–259, 149–162.

Qi, Y.Q., Hu, R.Z., Gao, J.F., Leng, C.B., Gong, H.T., Gao, W., 2020. Late Mesozoic oxidized magma for porphyry Ag mineralization: A comparative study from mineralized and barren granite porphyries in the Lengshuikeng Ag-(Pb-Zn) deposit, South China. J. Asian Sci. 104180.

Righter, K., Leeman, W.P., Hervig, R.L., 2006. Partitioning of Ni, Co and V between spinel-structured oxides and silicate melts: Importance of spinel composition. Chem. Geol. 227, 1–25.

Rusk, B.G., Oliver, N.H.S., Zhang, D., Brown, A., Lilly, R., Jungmann, D., 2009, Compositions of magnetite and sulfdes from barren and mineralized IOCG deposits in the eastern succession of the Mt. Isa inlier, Australia: Geological Society of America (GSA) Annual Meeting, Portland, Oregon, October 18–21, 2009, Proceedings, 1- 84.

Seward, T.M., 1976. The stability of chloride complexes of silver in hydrothermal solutions up to 350 °C. Geochim. Cosmochim. Acta 40 (11), 1329–1341.

Shang, L.B., Fan, W.L., Deng, H.L., 2003. An experimental study on paragenesis and separation of sliver, lead and zinc in hydrothermal solutions. Acta Mineral. Sinica 23 (1), 31–36 (in Chinese).

Shang, L.B., Fan, W.L., Hu, R.Z., Deng, H.L., 2004. A thermodynamic study on paragenesis and separation of sliver, lead and zinc in hydrothermal solutions. Acta Mineral. Sinica 24 (1), 81–86 (in Chinese).

Shu, L.S., Charvet, J., 1996. Kinematic and geochronology of the Proterozoic Dongxiang-Shexian ductile shear zone (Jiangnan region, South China). Tectonophysics 267 (1–4), 291–302.

Shu, L.S., Zhou, X.M., Deng, P., Wang, B., Jiang, S.Y., Yu, J.H., Zhao, X.X., 2009. Mesozoic tectonic evolution of the Southeast China Block: New insights from basin analysis. J. Asian Earth Sci. 34, 376–391.

Singoyi, B., Danyushevsky, L., Davidson, G.J., Large, R., Zaw, K., 2006. Determination of trace elements in magnetites from hydrothermal deposits using the LA ICP-MS technique. SEG 2006: Wealth Creation in the Minerals Industry. Society of Economic Geologists.

Stefansson, A., Seward, T.M., 2003. Experimental determination of the stability and stoichiometry of sulphide complexes of silver(I) in hydrothermal solutions to 400 °C at 500 bar. Geochim. Cosmochim. Acta 67, 1395–1413.

Su, H.M., Mao, J.W., He, X.R., Lu, R., 2013. Timing of the formation of the Tianhuashan Basin in northern Wuyi as constrained by geochronology of volcanic and plutonic rocks, Science China. Earth Sci. 56, 940–955.

Su, H.M., Mao, J.W., Santosh, M., Xie, G.Q., 2014. Petrogenesis and tectonic significance of Late Jurassic–Early Cretaceous volcanic-intrusive complex in the Tianhuashan basin, South China. Ore Geol. Rev. 56, 566–583.

Sun, J.D., Luo, X.Q., Zhang, X.H., Zhang, C.M., Li, C.H., Yu, M.G., Zhu, Y.P., Zong, W., 2014. A genetic study of Fe-Mn carbonate breccias in the Lengshuikeng Ag-Pb-Zn deposit, Jiangxi Province. Geol. China 41 (2), 484–496.

Van Baalen, M.R., 1993. Titanium mobility in metamorphic systems: a review. Chem. Geol. 110, 233–249.

Wang, C.M., Xu, Y.G., Wu, G.G., Zhang, D., Yang, L., Liu, J.G., Wan, H.Z., Di, Y.J., Yu, X.Q., He, M.Y., Zhang, Y.Y., 2011. C, O, S and Pb isotopes characteristics and sources of the ore metals of the Lengshuikeng Ag-Pb-Zn ore field, Jiangxi. Earth Sci. Front. 18, 179–193 (in Chinese).

Wang, C.M., Zhang, D., Wu, G.G., Santosh, M., Zhang, J., Xu, Y.G., Zhang, Y.Y., 2014. Geological and isotopic evidence for magmatic-hydrothermal origin of the Ag–Pb–Zn deposits in the Lengshuikeng District, east-central China. Miner. Deposita 49, 733–749.

Wang, Y.J., Fan, W.M., Zhang, G.W., Zhang, Y.H., 2013. Phanerozoic tectonics of the South China Block: key observations and controversies. Gondwana Res. 23 (4), 1273–1305.

Wang, C.M., Wu, G.G., Zhang, D., Luo, P., Di, Y.J., Yu, X.Q., 2010. Regional metallogenic characteristics and mineralizing pedigree in northeastern Jiangxi. Global Geol. 29, 588–600 (in Chinese).

Whitney, J.A., Hemley, J.J., Simon, F.O., 1985. The concentration of iron in chloride solutions equilibrated with synthetic granitic compositions; the sulfur-free system. Econ. Geol. 80, 444–460.

Williams-Jones, A.E., Migdisov, A.A., 2014. Experimental constraints on the transport and deposition of metals in ore-forming hydrothermal systems. Soc. Econ. Geologists 18, 77–96.

Yang, M.G., Wang, F.N., Zeng, Y., Lai, X.P., Huang, S.B., Zhou, H., 2004. In: Metallogenic Geology in the North Part of Jiangxi Province. China Land Press, Beijing, pp. 1–186 (in Chinese).

Yu, X.Q., Wu, G.G., Zhang, D., Di, Y.J., Dai, Y.P., Qiu, J.T., 2008. Thrust nappe structure and its ore-controlling effects in the North Wuyi area. Geol. Bull. China 27 (10), 1667–1677 (in Chinese).

Yu, X.Q., Wu, G.G., Zhao, X.X., Zhang, D., Di, Y.J., Qiu, J.T., Dai, Y.P., Li, C.L., 2012. New geochronological data from the Paleozoic and Mesozoic nappe structures, igneous rocks, and molybdenite in the North Wuyi area, Southeast China. Gondwana Res. 22 (2), 519–533.

Yu, Z.Z., Cao, S.H., Luo, X.H., 2008. Evaluation and prospective of reserves of copperpolymetallic mineral resources in Wuyishan mountain metallogenic belt, Jiangxi province. Resour. Surv. Environ. 29 (4), 270–278 (in Chinese).

Zhong, R., Brugger, J., Chen, Y., Li, W., 2015a. Contrasting regimes of Cu, Zn and Pb transport in ore-forming hydrothermal fluids. Chem. Geol. 395, 154–164.

Zhong, R., Brugger, J., Tomkins, A.G., Chen, Y., Li, W., 2015b. Fate of gold and base metals during metamorphic devolatilization of a pelite. Geochim. Cosmochim. Acta 171, 338–352.

Zhou, M.F., Yan, D.P., Kennedy, A.K., Li, Y., Ding, J., 2002. SHRIMP U-Pb zircon geochronological and geochemical evidence for Neoproterozoic arc-magmatism along the western margin of the Yangtze block, South China. Earth Planet. Sci. Lett. 196, 51–67.

Zuo, L.Y., Hou, Z.Q., Song, Y.C., Meng, X.J., Yang, Z.S, 2009. Study of the ore-forming fluid in the Lengshuikeng Ag-Pb-Zn porphyry deposit. Acta Geosci. Sinica 30 (5), 616–626.

Zuo, L.Y., Hou, Z.Q., Meng, X.J., Yang, Z.M., Song, Y.C., Li, Z., 2010. SHRIMP U-Pb zircon geochronology of the ore-bearing rock in the Lengshuikeng porphyry type Ag–Pb–Zn deposit. Geol. China 37, 1450–1456 (in Chinese).